JGR Atmospheres

RESEARCH ARTICLE
10.1029/2022JD037064

Impact of Cyclone-Cyclone Interaction on Lake-Effect Snowbands: A False Alarm

Zuohao Cao[1], Qin Xu[2], and Da-Lin Zhang[3]

[1]Meteorological Research Division, Environment and Climate Change Canada, Toronto, ON, Canada, [2]NOAA/National Severe Storms Laboratory, Norman, OK, USA, [3]Department of Atmospheric and Oceanic Science, University of Maryland, College Park, MD, USA

Key Points:

- Impacts of cyclone-cyclone interactions on a false alarm with the prediction of doubled snowfall amount over Lake Erie are examined
- Positions of two cyclones are poorly predicted by the operational model, leading to errors in their induced winds over Lake Erie
- Over-predictions of conditional symmetric instability result in the false alarm of the lake-effect snowfall over Lake Erie

Correspondence to:
Z. Cao,
zuohao.cao@ec.gc.ca

Citation:
Cao, Z., Xu, Q., & Zhang, D.-L. (2023). Impact of cyclone-cyclone interaction on lake-effect snowbands: A false alarm. *Journal of Geophysical Research: Atmospheres*, *128*, e2022JD037064. https://doi.org/10.1029/2022JD037064

Received 3 MAY 2022
Accepted 10 DEC 2022

Author Contributions:
Formal analysis: Zuohao Cao, Qin Xu
Investigation: Zuohao Cao, Qin Xu, Da-Lin Zhang
Writing – original draft: Zuohao Cao
Writing – review & editing: Zuohao Cao, Qin Xu, Da-Lin Zhang

Abstract In this study, the impacts of two cyclone interactions with the environmental flow and with each other on a heavy winter snowfall event over the Great Lakes region are examined by applying a recently-developed diagnostic tool to a lake-effect snowstorm. This winter snowfall event was a false alarm by the Canadian operational model, in which the predicted lake-effect snowfall at the lee side of Lake Erie doubles the observed. The false alarm involves the interactions of two cyclones, whose relative locations are poorly predicted, leading to inaccurate prediction of their induced winds and interactions over Lake Erie at both low and upper levels. In particular, at 1,000 hPa, the cyclone-induced winds and their interactions over Lake Erie caused colder and drier air over warm-moist open-water lake surface that is favorable for more latent heat flux deriving from the lake in the model than in the real atmosphere. At 500 hPa, the location errors of the model predicted cyclones reversed the cyclone-induced winds over Lake Erie from mainly southerly to northerly, especially during the intense snowfall period. An analysis of the conditional symmetric instability (CSI) index over Lake Erie reveals that the operational model systematically over-predicts CSI, more significantly during the intense snowfall period. As a result, the operational model prediction makes a false alarm of a lake-effect snowfall event with large errors in precipitation intensity. Future improvements in operational model predictions are also suggested.

Plain Language Summary We have examined the impacts of two cyclone interactions on a heavy winter snowfall event over the Great Lakes region by applying a recently-developed diagnostic tool to a lake-effect snowstorm. This winter snowfall event was a false alarm by the Canadian operational model, with a prediction of doubled snowfall amount observed over Lake Erie. The false alarm involves the interactions of two cyclones, whose relative locations are poorly predicted, leading to inaccurate prediction of their induced winds and interactions over Lake Erie at both low and upper levels. At the low level, the cyclone-induced winds and their interactions over Lake Erie caused colder and drier air over warm-moist open-water lake surface that is favorable for more latent heat flux deriving from the lake in the model than in the real atmosphere. At the upper level, the location errors of the model predicted cyclones reversed the cyclone-induced winds over Lake Erie from mainly southerly to northerly, especially during the intense snowfall period. An analysis of the conditional symmetric instability (CSI) index over Lake Erie reveals that the operational model systematically over-predicts CSI, more significantly during the intense snowfall period. Because of the above reasons, the false alarm of lake-effect snowfall results.

1. Introduction

Interactions between two or multiple cyclones (via the induced flow by each cyclone that advects other cyclones) play an important role in predicting precipitation through changes of their track and intensity, as well as their associated dynamics and thermodynamics (e.g., Cao et al., 2019; Cao & Zhang, 2016). Prediction errors in surface cyclone-cyclone interactions can therefore lead to disappointing predictions of severe precipitation events. For example, Cao et al. (2019) have successfully diagnosed the interactions of three mid-latitude cyclones responsible for failure to predict a severe rainfall in summer using their recently developed method. This failed prediction of the summer severe rainfall event is due to a responsible cyclone predicted by the model moving away from the observed location as revealed by the diagnosed interactions and becoming unfavorable to the severe rainfall (Cao et al., 2019; Cao & Zhang, 2016). Therefore, cyclone-cyclone and cyclone-environment interactions are critical in diagnosing prediction errors in precipitation distribution, which can further lead to precipitation intensity and timing errors (e.g., Cao et al., 2019; Cao & Zhang, 2004; Cao & Zhang, 2016).

Yet, little research has been documented in the literature on winter precipitation errors resulting from surface cyclone-cyclone and cyclone-environment interactions, especially in highly populated areas such as the Great Lakes region, although the previous studies on winter snowstorms in the Great Lakes region are mainly associated with synoptic scale cyclones (e.g., Isard et al., 2000; Keshishian et al., 1994), fronts, troughs, baroclinic zones (e.g., Keshishian et al., 1994; Kocin & Uccellini, 1990; Payer et al., 2011), and forced ascent over low level cold outflows from cold surface anticyclones (e.g., Kocin & Uccellini, 1990). The earlier studies also examine the impacts of 500-hPa trough merger (e.g., Lai & Bosart, 1988), mesoscale instability (e.g., Milrad et al., 2011), and lake effect (e.g., Ballentine et al., 1998; Burnett et al., 2003; Ellis & Johnson, 2004; Kristovich et al., 2000; Laird et al., 2003; Mann et al., 2002; Murphy, 1989; Niziol, 1987; Norton & Bolsenga, 1993) on the severe snowfalls.

Recent lake-effect studies also include one-way coupled air-lake model simulations to improve representation of lake temperature and ice coverage leading to better turbulent heat fluxes over the lake and snow water equivalent in the downwind areas (e.g., Fujisaki-Manome et al., 2020), the sensitivity of lake-effect snowfall to lake ice cover and temperature as well as the interactions among lake surface fluxes, the large-scale flow, the local lake shore geography and inland topography (e.g., Wright et al., 2013), and triggering mechanisms such as topographic lifting (e.g., Campbell et al., 2016; Campbell & Steenburgh, 2017), frictional lifting, thermal lifting and dynamic lifting (Steenburgh & Campbell, 2017). Field campaigns (e.g., Kristovich et al., 2000), on the other hand, could be beneficial to better understand various scales of phenomena and their interactions associated with lake-effect snowstorms.

Usually, a lake-effect snowfall event is identified when it has an elongated band of precipitation downwind of the lake whereas a lake-enhanced event is recognized in association with a convective cellular shaped precipitation originated or enhanced over the open water, and other convective activity upwind of the lake (e.g., Tardy, 2000). The detailed definitions of lake effect precipitation can also be found in Wiggin (1950) and Niziol (1987). As pointed out by Niziol et al. (1995) in their classification of five types of lake-effect snowfall, snowbands can be either single or multiple bands, and their orientations can be parallel or perpendicular to a lake long axis, but the most intensive lake-effect precipitation is associated with a single elongated band as described in Niziol et al. (1995).

In this study, we investigate a severe lake-effect snowfall event associated with two cyclones, referred to as cyclone A, and B, respectively (Figure 1), and their interactions. This event occurred on the lee sides of Lake Erie and Lake Ontario during the open water period of 19–21 November 2016. This was the first significant snowfall event of the season in most areas of Pennsylvania. The severe snowfall event led to more than 27,000 power outages in Rochester, New York, and highway closures as well as numerous traffic accidents. The severe lake-effect snowfall event was documented in Storm Events Database of NOAA's National Centers for Environmental Information (https://www.ncdc.noaa.gov/stormevents/), and identified by NOAA National Weather Service in Buffalo, New York (https://www.weather.gov/buf/lesEventArchive?season=2016-2017&event=A). Based on the definition of lake-effect snowfall (Niziol, 1987; Wiggin, 1950), cyclone A was mainly responsible for the snowfall at lee side of lakes when it was traveling between the Great Lakes and James Bay, Canada starting around 1200 UTC 19 November 2016 (Figures 1 and 2). The snowband at the lee of Lake Erie was oriented mainly in east-west direction parallel to south shoreline of Lake Erie (Figure 2), which was different from the northeast-southwest oriented precipitation band associated with a northeast-moving cyclone A and its interaction with cyclone B (see Figure 1). As will be shown herein, the interaction of the two extratropical cyclones A and B played a major role in generating this heavy snowfall event (Figures 1 and 2).

Traditionally, a lake-effect snowfall event is defined as one surface low-pressure center (associated with a 500-hPa low pressure system) tracking from west to east between the Great Lakes and James Bay, Canada, which carries cold and dry air over warm and moist lake surface to generate sensible and latent heat fluxes and produce lake-effect snowfall at lee of the lake (Niziol, 1987; Wiggin, 1950). This simplified version of one-surface-cyclone pattern allows one to focus on a key specific weather system, which is preferable when no tools are available to deal with interactions between two or more cyclones and their impacts on lake-effect precipitation. Since the lake-effect precipitation associated with two or more cyclones occurs from time to time, the newly developed diagnostic method described in Cao et al. (2019) is particularly appropriate to examine the effects of two or more cyclones and their interactions on lake-effect precipitation, with emphasis on severe precipitation having high impacts on society.

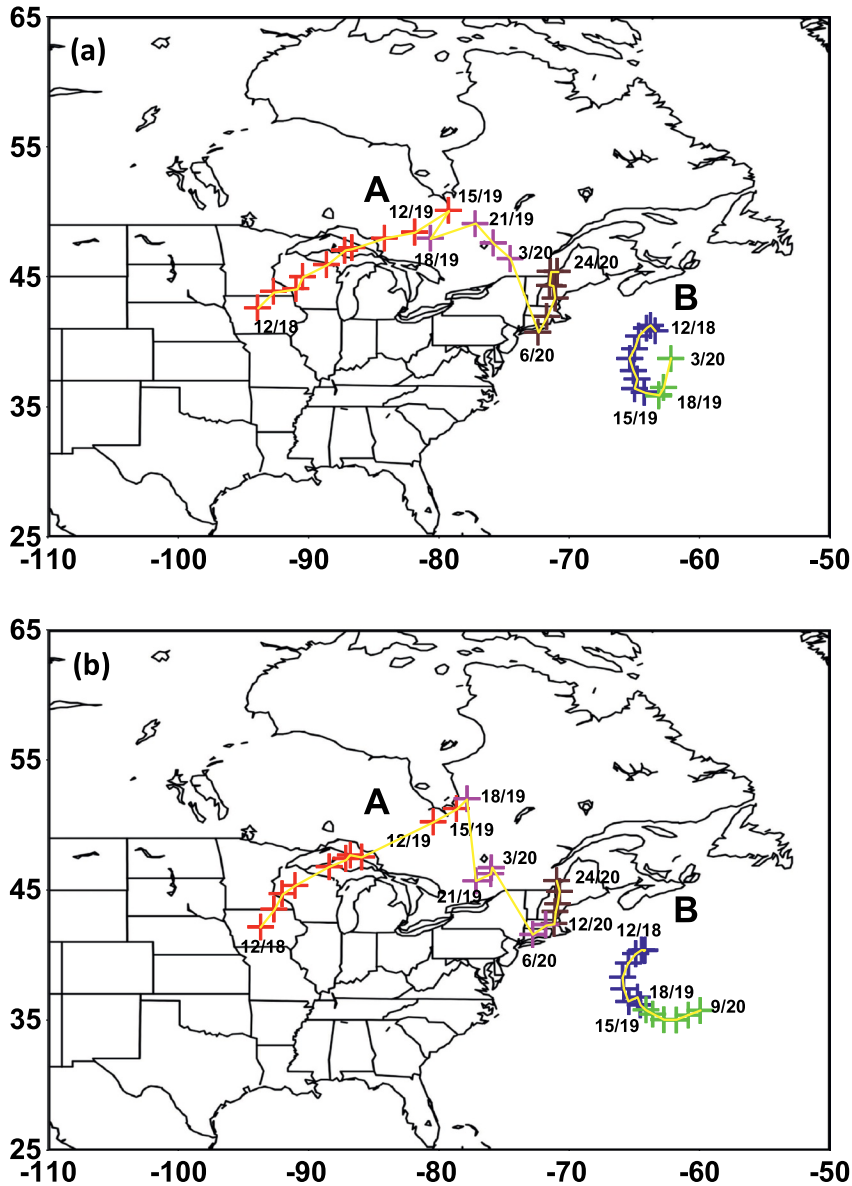

Figure 1. Tracks of cyclones A and B at 1,000 hPa based on (a) the NARR analysis and (b) the GEM regional model predictions at hours (UTC)/day labeled along their paths. Cyclones A and B are, respectively, denoted by red and blue crosses before they merge, by pink and green crosses after they merge but still remain two separate low centers. Brown crosses represent locations of cyclone centers after the two centers merge into a single center.

Since development of lake-effect snowfall is highly dependent on advection of cold and dry air over a warm and moist lake surface, wind magnitude and direction over the lake are critical for lake-effect snowfall. It is therefore important to examine the wind due to two or more cyclones and their interactions when these cyclones simultaneously show up in a lake-effect snowfall event. To our knowledge, this type of interactions has not been taken into consideration in scientific literature and forecast practice. By applying Cao et al. (2019)'s diagnostic method, we are able to extract rotational and divergent flows induced by cyclones or low-pressure systems at any level. At the cyclone scale, rotational component usually dominates in the horizontal velocity, whereas divergent component is large in the boundary layer. The two components play different roles in cyclone-cyclone interactions. That is, cyclonic rotation tends to displace fluid particles or disturbance cyclonically, while convergence tends to attract them into the cyclone, and also indicates where vertical motion is. It is expected that investigation of cyclones and their interactions will further inform errors in wind magnitude and direction associated with lake-effect snowfall; this could potentially lead to accurate quantitative predictions.

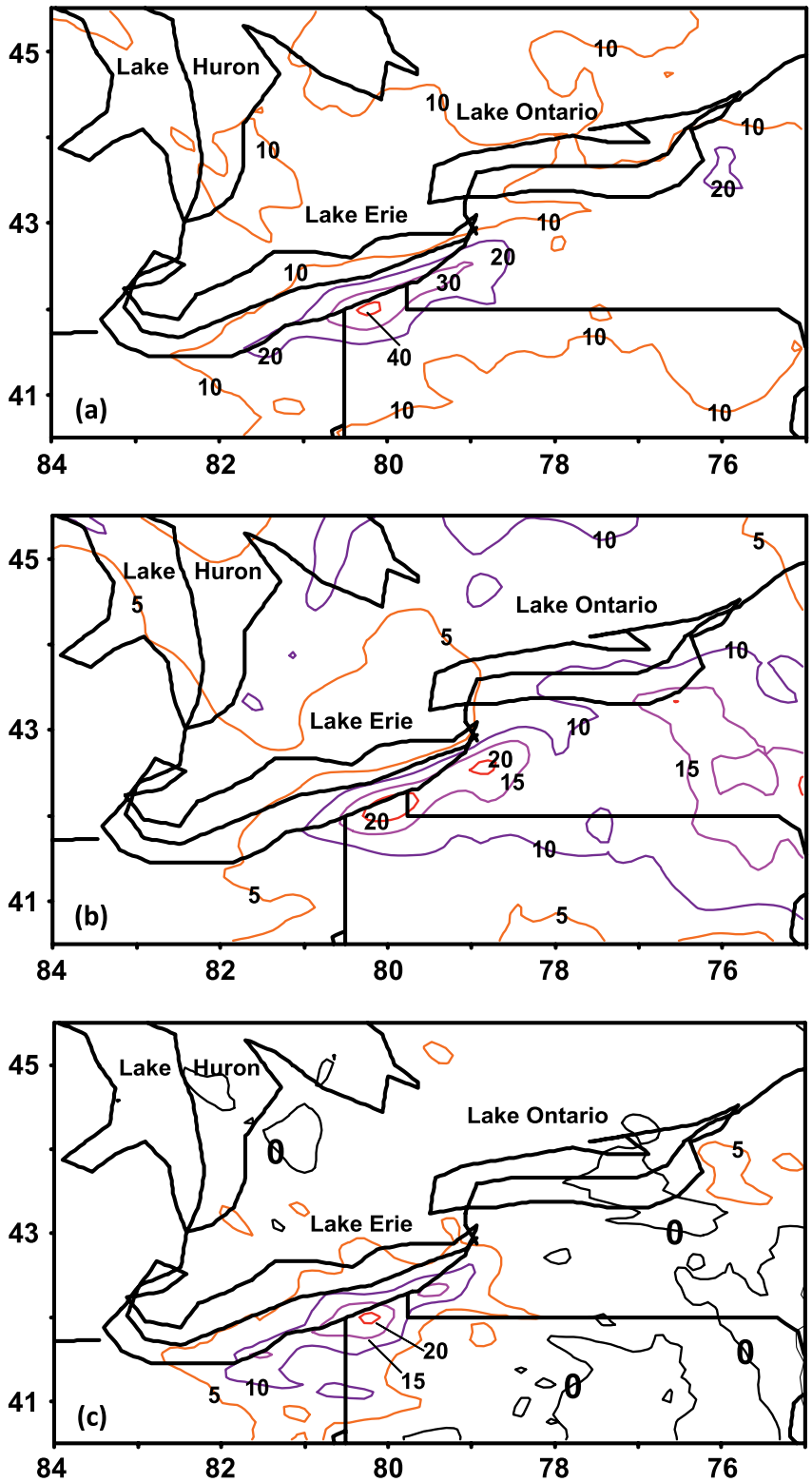

Figure 2. Precipitation accumulation (mm) for the period of 1200 UTC 19 to 1200 UTC 20 November of (a) the GEM model predicted, (b) the CaPA analyzed, and (c) differences between the GEM model predicted and the analyzed.

The event examined in this study is a false alarm of a severe lake-effect snowfall event because the Canadian operational model predicts a lake-effect snowfall band at the lee side of Lake Erie with a rate of about 40 cm day^{-1} (Figure 2a), exceeding the winter storm threshold of 25 cm in 24 hr (based on Ontario Storm Prediction Center's (OSPC) definition), whereas the observed maximum snowfall rate is about 20 cm day^{-1} (Figure 2b).

This case study was further motivated after we found overprediction of daily precipitation over southern Ontario (84°–75°W and 41°–47°N) by the Canadian operational model (i.e., GEM model) during the period of June 2016 to May 2017. Specifically, as shown in Figure 2a of Cao et al. (2022), the domain- and monthly-averaged bias in daily quantitative precipitation forecasts (QPFs) is positive for the GEM model (with a 10-km horizontal grid spacing) over the entire year, implying over-prediction of the daily precipitation when comparing to Canadian Precipitation Analysis (CaPA)'s daily accumulation (Figure 2a of Cao et al. (2022)). Therefore, the GEM-overpredicted precipitations examined here are quite representative of the current status of the GEM performance in daily QPF. These GEM over-predictions include QPF errors in location, intensity, and timing. Particularly for lake-effect snowfall, incorrect wind predictions in location and intensity can lead to corresponding errors in the advection of cold dry air over a warm moist lake surface and the lake-effect snowfall.

Accurate prediction of winter snowfall over the Great Lakes region is still challenging, especially for its locations and amount (Fujisaki-Manome et al., 2022). Regarding winter weather forecasts in Ontario, Canada, OSPC received the public complaints mostly concerning false alarms in forecasting snowfall events, especially lake-effect and/or lake-enhanced snowfall. A false alarm refers to a forecasted event that did not occur. The false alarm rate (FAR) measures the portion of predicted events that did not happen (Barnes et al., 2007; Brotzge et al., 2011). Currently, false alarms in forecasting severe snowfall events are still among the key problems facing the forecast communities (e.g., Barnes et al., 2007). For example, the 2004–2005 U.S. FAR for winter storm warnings was 0.31 (e.g., Barnes et al., 2007), that is, 3 out of 10 warnings failed.

Besides dynamics associated with cyclone induced winds at the low and middle levels, we also examine the vertically integrated dynamic and thermodynamic processes at all possible levels. To this end, we looked the conditional symmetric instability (CSI) index to see if model-resolvable convection (mostly slantwise but becoming upright in the limit of vanishing thermal wind shear) could be responsible for the development of snowbands over Lake Erie. Here, the CSI index informs three aspects, that is, instability, moisture availability, and lifting conditions.

According to the theoretical analysis of symmetric instability (SI) in Xu and Clark (1985), the SI that generates slantwise convection as an extension of convective instability (CI) when the basic-state parameter space is extended to include the unidirectional thermal wind shear parameter. Hence, SI includes CI, and CI is a special case of SI in the limit of vanishing thermal wind shear (with unstable vertical stratification). In the presence of unidirectional thermal wind (as observed in the real atmosphere such as in and around Lake Erie as a case study presented in this paper), convection generated by unstable moist vertical stratifications will not be generally and exactly upright (as depicted by the classic theory of conditional CI (CCI) (Kuo, 1961; Lilly, 1960), but should be slantwise as shown by the analytical solutions of slantwise moist convections generated by CSI in Xu (1986).

Based on the above theoretical understanding, CSI should include a specific type of CCI and, as explained above, and this type of CCI is a degeneration of CSI in the limit of vanishing unidirectional thermal wind shear. For practical applications (as considered later in this paper), such a degeneration (from CSI to CCI) can be considered loosely to occur when the thermal wind shear is roughly unidirectional but becomes very weak or virtually vanishes. Here, as a caveat, it is necessary to point out that CSI is not yet generalized to include or apply to other types of moist convection generated (often in non-banded forms) by CCI in environmental flows that differ substantially from unidirectional thermal winds (as also observed in the real atmosphere). In other words, it is sufficient to just consider CCI (and unnecessary to consider CSI) in the boundary layer if convection is little or virtually not affected by baroclinicity associated with thermal wind. In this case, the CSI release index [defined later in Equation (3)] reduces to a CCI release index [with the moist potential vorticity (PV) defined in Equation (4) reduces to $f\partial_z\theta_e/\rho$], so this reduced CSI release index remains valid and useful for the application considered in this paper.

With the above caveat for the explained inclusion of CCI into CSI, we notice that CSI has been well studied as an indicator for the formation of snowbands and rainbands (e.g., Bennetts & Hoskins, 1979; Clark et al., 2002; Lussky, 1989; Xu, 1986, 1992) but has not yet been studied specifically for or applied to snow bands associated with lake-effect.

Therefore, the objectives of this study are to (a) diagnose cyclone-cyclone and cyclone-environment interactions and examine their impacts on the lake-effect snowfall event using our newly-developed method; and (b) explore possible reasons behind this false-alarm in order to provide physical understanding of why the operational models fail. In particular, the development of CSI and its possible role in forming the lake-effect snowbands are examined.

The next section describes the data and methodology used in this study. The following three sections analyze the differences between the observations and the model predictions in terms of cyclone movements and locations (Section 3), cyclone-induced flows (Section 4), and CSI (Section 5). More attention will be given to the differences in relation to the false alarm of the severe lake-effect snowfall. Relevant discussions are given in Section 6. Concluding remarks and recommendations are presented in the final section.

2. Data and Methodology

The datasets employed in this study include: (a) the hourly operational GEM (Global Environmental Multi-scale) regional model (Côté et al., 1998) predictions with a 10-km horizontal grid spacing and 58 vertical levels, retrieved from the archive at the Canadian Meteorological Center (CMC); (b) the 3 hourly North American Regional Reanalysis (NARR) with a horizontal grid spacing of 32-km and 29 constant pressure levels that are archived at the National Centers for Environmental Prediction (NCEP) (Mesinger et al., 2006); (c) the Canadian Precipitation Analysis (CaPA) data (Lespinas et al., 2015; Mahfouf et al., 2007). In the most recent version of the CaPA analysis, Canadian, and U.S. radar data have been assimilated into the operational GEM regional model with 10 km horizontal grid spacing in addition to the rain gauge data (Fortin et al., 2015; Lespinas et al., 2015). The CaPA analysis of precipitation is assimilated daily at 1200 UTC. As a result, the GEM model 1200 UTC run is assessed for its prediction of lake-effect snowfall.

The NARR analysis has been widely used (e.g., Bukovsky & Karoly, 2007; Carrera et al., 2009; Langlois et al., 2009; Milrad et al., 2011). Since the NARR analysis assimilates precipitation observations over the United States and other observations in the North American, it provides a much better representation of precipitation and other fields than other reanalyses such as NCEP-DOE, ERA-40, and CPC (Bukovsky & Karoly, 2007). The NARR mean seasonal precipitation amount is very close to the observed throughout the year, although it somewhat underestimates extremes and overestimates lighter events in the eastern half of the United States (Becker and Berbery, 2009). Because the NARR does not assimilate the observed precipitation over Canada, we use the CaPA analysis instead of the NARR precipitation analysis. Ideally, we should use high-resolution observations to verify the GEM regional model predicted fields. Unfortunately, there are no such routine observational data available. For example, a low pressure system center is usually not located at any given climate station so that a central MSLP of the weather system cannot be verified against the station observations. Our choice is therefore to use the high resolution NARR reanalysis data that are independent of the GEM predictions, as typically required.

We apply our recently developed method (Cao et al., 2019), as an improvement to the classical point vortex model (Batchelor, 1980; Ziv & Alpert, 1995), to extract both the rotational and divergent parts of the flow induced by a cyclone or low-pressure system on a given vertical level. Based on Cao et al. (2019), in a two-dimensional space of $\mathbf{x}$ on a given vertical level (such as a constant pressure surface), the rotational velocity, denoted by $\mathbf{v_r} \equiv (u_\mathbf{r}, v_\mathbf{r})$, induced by the vorticity, denoted by ζ, within the core area of a cyclone or low-pressure system can be formulated as

$$\mathbf{v_r}(\mathbf{x}) = (2\pi)^{-1} \int_s d\mathbf{x}'\zeta(\mathbf{x}')\mathbf{k} \times (\mathbf{x} - \mathbf{x}')/|\mathbf{x} - \mathbf{x}'|^2, \tag{1}$$

where $\int_s d\mathbf{x}'$ denotes the integration over the core area S and $\mathbf{k}$ is a unit vector in the vertical direction. Although $(\mathbf{x} - \mathbf{x}')/|\mathbf{x} - \mathbf{x}'|^2$ on the right-hand side of Equation (1) becomes singular as $\mathbf{x}' = \mathbf{x}$, it is still integrable in $\mathbf{x}'$ using the grid-staggering discretization scheme with no singularity involved (Cao et al., 2019; Cao & Xu, 2011). Similarly, the divergent velocity, denoted by $\mathbf{v_d} \equiv (u_\mathbf{d}, v_\mathbf{d})$, induced by the divergence, denoted by α, within the core area can be written as

$$\mathbf{v_d}(\mathbf{x}) = (2\pi)^{-1} \int_s d\mathbf{x}'\alpha(\mathbf{x}')(\mathbf{x} - \mathbf{x}')/|\mathbf{x} - \mathbf{x}'|^{2.} \tag{2}$$

Again, using the grid-staggering discretization scheme can avoid singularity at $\mathbf{x}' = \mathbf{x}$ on the right-hand side of Equation (2) (Cao et al., 2019; Cao & Xu, 2011).

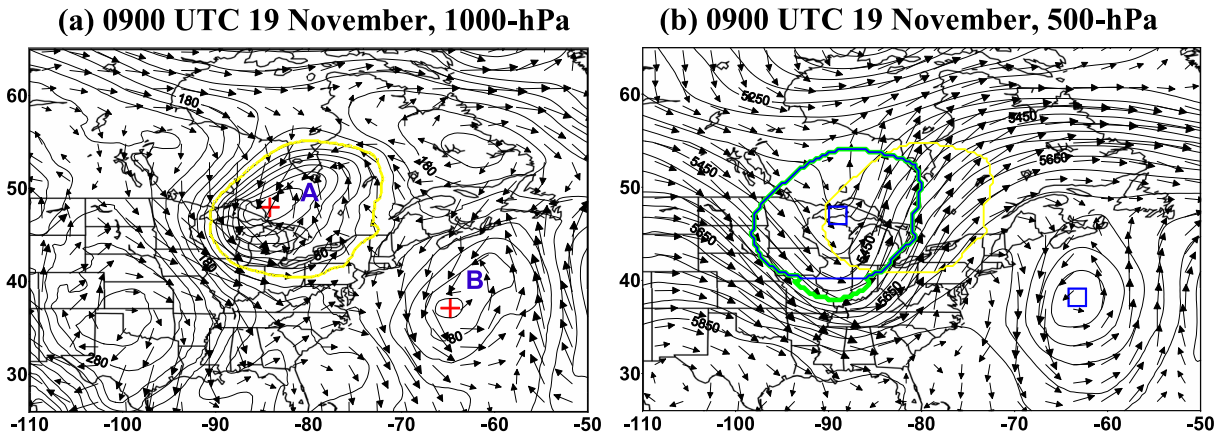

Figure 3. NARR 1,000-hPa (left column) and 500-hPa (right column) geopotential height (black-contoured at every 20 and 40 m for 1,000-hPa and 500-hPa, respectively) and horizontal winds vectors with a wind speed range of (a) 1.0–21.0 m s^{-1} and (b) 1.0–51.2 m s^{-1} at 0900 UTC 19 November 2016. The red "+" sign denotes the 1,000-hPa vortex center of cyclones A and B, and a yellow loop encircles the 1,000-hPa vortex core area. A small blue box marks the center of the 500-hPa vortex core (encircled by a blue loop) projected from the 1,000-hPa vortex core (encircled by a yellow loop), and a green loop encircles the finally extended 500-hPa vortex core (determined through the additional second step).

It should be noticed as a caveat that the rotational velocity induced by the vorticity inside the core area *S* of a cyclone is nondivergent (with zero divergence) and irrotational (with zero vorticity) outside the core area, although it rotates cyclonically around the core outside the core area. Similarly, the divergent velocity field (also called divergent flow) induced by the divergence inside the core area is irrotational (with zero vorticity) and nondivergent (with zero divergence) outside the core area, although it flows toward and into the core area.

According to Equations 1 and 2, the rotational and divergent flows induced by a cyclone can be realistically extracted from the total flow by inverting the vorticity and the divergence in a well-defined vortex core area of the cyclone. For the two low-pressure systems A and B considered in this paper, each low-pressure system forms an elongated surface cyclone at 1,000 hPa (Figure 3a). Following Cao et al. (2019) and the flowchart in their Figure 2, for each surface cyclone the vortex core area can be defined as an area enclosed by the outmost iso-geopotential height loop at 1,000 hPa (e.g., the yellow loop in Figure 3a) and the vortex center is determined by the minimum geopotential height inside the vortex core (the red "+" sign in Figure 3a).

At 500 hPa, however, only one low-pressure system B forms a cyclone (with a sufficiently large outmost iso-geopotential height loop to determine the vortex core area), situated offshore in the Atlantic Ocean far east of the Great Lake area (Figure 3b). This cyclone center and its vortex core area are determined in the same way as described in Cao et al. (2019). The other low-pressure system A, located over the central US and Canada, forms a deep trough at 500 hPa with no iso-geopotential height loop (until the trough was cut off into an isolated low at a later time, not shown), and its vortex was implicitly embedded in the highly curved total flow around the 500-hPa trough.

The center of this implicit vortex cannot be rigorously defined but can be searched along the trough line and determined as the point with a maximum change of wind direction cross the trough line. This process involves the following steps: (a) searching a maximum change of wind direction at adjacent grid points along a direction approximately perpendicular to a trough (in this case it is in a zonal direction); (b) repeating this process in the implicit vortex area, we obtain a set of two dimensional coordinates, and link these points and we have a trough line; (c) searching a maximum change of wind direction along the trough line, we obtain the two dimensional coordinates of the center of the implicit vortex. This center is considered to be the center of the 500-hPa vortex core area, and its horizontal distance to the geometric center of the 1,000-hPa vortex core area is used to compute the horizontal displacement for projecting the vortex core area from 1,000 to 500 hPa (e.g., the blue loop in Figure 3b). In summary, the 500-hPa vortex core area associated with the trough is determined through the following two steps: (a) Compute the aforementioned horizontal displacement and use it to project the 1,000-hPa vortex core area to 500 hPa in the same way as described in Section 4 of Cao et al. (2019) except that the horizontal displacement is computed differently as explained earlier. (b) Extend the projected vortex core area southward to include the deep trough area extruded from the projected vortex core area, while the extruded trough area must

be enclosed by the southern boundary of the 500-hPa projected vortex core and the southernmost concave contour of geopotential height extended from the 500-hPa projected vortex core. Note that the southernmost concave contour must intersect the southern boundary of the 500-hPa projected vortex core twice at its west and east ends of the concave contour. With this additional second step, the finalized 500-hPa vortex core area can properly cover the deep trough at 500 hPa (e.g., the green loop in Figure 3b).

To further explore if there are differences of CSI responsible for different development of snowbands over Lake Erie between the NARR and the GEM, we calculate the CSI release index since it takes account of both dynamic and thermodynamic components and is a likely cause for the formation of band precipitation (e.g., Bennetts & Hoskins, 1979; Xu, 1986, 1992). In this study, the CSI release index includes atmospheric instability, moisture availability, and lifting mechanism (e.g., Huang et al., 2019):

$$\begin{cases} MPV < 0 \\ RH > RHc, \\ W > 0 \end{cases} \tag{3}$$

where MPV is the moist PV, defined as

$$MPV = \frac{1}{\rho}\vec{\zeta}_a \cdot \nabla\theta_e, \tag{4}$$

in which $\vec{\zeta}_a$, θ_e, and ρ are the absolute vorticity vector, equivalent potential temperature and density, respectively. RH is relative humidity and W is the vertical velocity. $MPV < 0$ is a necessary condition for CSI to occur (e.g., Cao & Cho, 1995; Xu, 1992; Zhang & Cho, 1992). To release CSI, sufficient moisture and lift conditions need to be present. Here, RHc is a relative humidity threshold value (85% in this study), which represents a near saturation condition, while upward motion ($W > 0$) is required for release of CSI.

For a given geographic location and atmospheric layer, we check if the criteria in (3) are satisfied at the same time and place. If yes, we account the index value as 1. We continuously check all the 15 vertical layers in the NARR to see how many levels satisfy these criteria, and then add them up to get the CSI index values for this geophysical location in the NARR. The CSI indexes for the GEM are computed in the same way as those for the NARR but the original 58 vertical levels in the GEM must be first coarsened through resampling to the same vertical levels (15 levels with a resolution of about 50-hPa) as those in NARR.

Milrad et al. (2011) examined the short-lived high-impact snowband event that occurred on 28 Jan. 2010 over the area between eastern Ontario and western Quebec. As shown in Fig. 6 of Milrad et al. (2011), below 850 hPa the region of CCI and the area of CSI are collocated in the same places. It is also observed that the area(s) of CSI are developed between about 850 hPa and 600 hPa (Figure 6 of Milrad et al., 2011). These instabilities are responsible for development of precipitation bands shown in Figure 1 of Milrad et al. (2011). In this case, the convections are nearly upright at low levels but become increasingly slantwise as they are extended upward into upper levels.

3. Movements and Locations of Cyclones A and B in NARR and GEM

3.1. Movements and Locations of Cyclones A and B Revealed From NARR

At 1200 UTC 18 November, that is, about 24 hr prior to the intense snowfall, two cyclones A and B were far away apart from each other (Figure 1a). At this time, the 1,000-hPa cyclone A was located over the central US and Canada to the west of the Great Lakes, while the 1,000-hPa cyclone B was situated offshore in the Atlantic Ocean far east of the Great Lakes (Figure 1a). Subsequently, they evolved differently during the following three periods.

During the first period from 1200 UTC 18 to 1500 UTC 19 November, cyclone A was moving northeastward while cyclone B was slowly moving southwestward, so the two cyclones were becoming close to each other (Figure 1a). Over the second period from 1500 UTC 19 to 0300 UTC 20 November, the center of cyclone A underwent a zigzag movement, that is, shifting first southwestward (from 1500 to 1800 UTC, see Figure 1a) and then moving back northeastward (from 1800 to 2100 UTC; see Figure 1a). After 0300 UTC 20 November, the center of cyclone A was moving southeastward and becoming increasingly close to cyclone B (Figure 1a). On

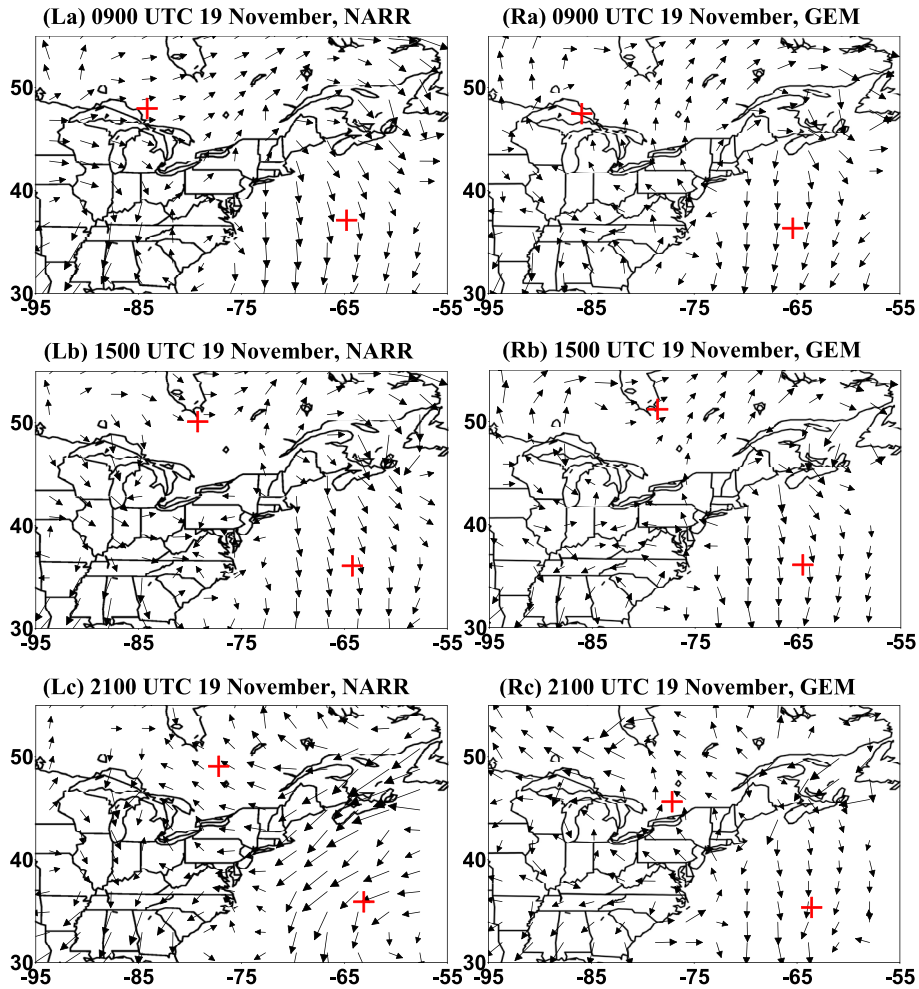

Figure 4. Same as Figure 3 except for left columns for NARR and right columns for GEM for the 1,000-hPa environmental flow (computed by subtracting the two cyclone induced flows from the total flow) plotted by black arrows with a wind speed range of (La) 1.0–22.5 m s^{-1}, (Lb) 1.0–19.8 m s^{-1}, (Lc) 1.0–20.7 m s^{-1}, (Ra) 1.0–22.1 m s^{-1}, (Rb) 1.0–19.3 m s^{-1}, and (Rc) 1.0–19.2 m s^{-1}. The red "+" signs denote the 1,000-hPa vortex center.

the other hand, cyclone B was quasi-stationary during the second phase but its center reversed its slow movement from southward to northward (Figure 1a). Over the third period from 0600 UTC to 2400 UTC 20 November, the two cyclones were merged into one cyclone with a single center (denoted by brown-colored "+" signs in Figure 1a). The movements of the two cyclones can be largely explained through their interactions with the environmental flow (Figure 4) over the first period and their mutual interactions for the subsequent two periods.

During the first period, the 500-hPa low-pressure system A was associated with a deep trough, as part of a large-amplitude baroclinic wave (e.g., Figures 5La and 5Lb). As this baroclinic wave was propagating eastward and northeastward following closely the 500-hPa environmental flow (see Figures 6La and 6Lb), the entire 1,000-hPa low-pressure system A was also moving eastward and northeastward (Figures 7La-7Lb, and 1a) following the baroclinic-wave propagation. This largely explains the movements of cyclone A over the first time period (Figure 1a). Furthermore, the center of 500-hPa trough in system A (blue box markers in Figures 6La and 6Lb) was vertically titled to the west or southwest of the 1,000-hPa vortex core area (red plus markers in Figures 6La and 6Lb). On the other hand, over the same period, system B formed a deep elongated cyclone from 1,000 to 500 hPa (Figures 7La-7Lb and 5La-5Lb). This elongated cyclone was nearly barotropic and quasi-stationary because it was located offshore in the Atlantic Ocean where the environmental flow was weak and nearly stagnated (see Figures 6La-6Lb). This was consistent with the slow movements of cyclone B during the first period (Figure 1a).

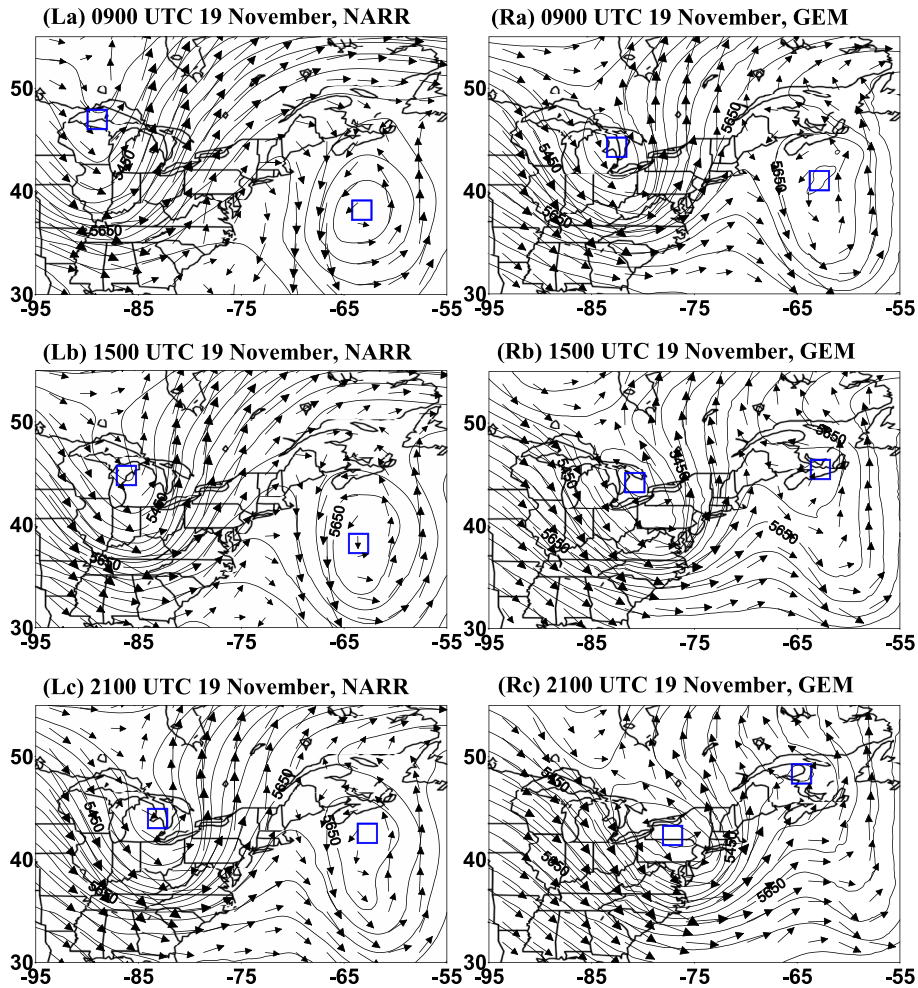

Figure 5. Same as Figure 3 except for left columns for NARR and right columns for GEM 500-hPa geopotential height and horizontal winds at (La and Ra) 0900 UTC, (Lb and Rb) 1500 UTC, and (Lc and Rc) 2100 UTC 19 November 2016. The wind speed ranges are, respectively, (La) 1.0–51.2 m s^{-1}, (Lb) 1.0–54.2 m s^{-1}, (Lc) 1.0–54.5 m s^{-1}, (Ra) 1.0–57.1 m s^{-1}, (Rb) 1.0–56.3 m s^{-1}, and (Rc) 1.0–52.1 m s^{-1}.

During the second time period from 1800 UTC 19 to 0300 UTC 20 November, cyclone A moved northeastward and then southeastward (see pink "+" signs in Figure 1a) and its elongated core area was gradually deformed into a core area with a new branch extruded southeastward toward cyclone B (see Figure 7Lc). This vortex core deformation caused the aforementioned zigzag shift of the center of cyclone A at the beginning of this second period (see pink "+" signs in Figure 1a), whereas the entire vortex core area of cyclone A was essentially moving southeastward with little zigzag shift (see a yellow loop in Figure 7Lc). Note that a triple point of cyclone A occurred between 0600 UTC to 1500 UTC 19 November, ahead of the second time period from 1800 UTC 19 to 0300 UTC 20 November when the zigzag motion of cyclone A happened. The southeastward movement of cyclone A manifested a southward deviation away from the northeastward baroclinic-wave propagation. This southward deviation can be largely explained by the southward advection caused by cyclone-B induced northerly flow (see the left column of Figure 8) that became strong enough to significantly affect the movement of cyclone A as cyclone A became sufficiently close to cyclone B during the second period. By the same token, the reversed northward movement of the center of cyclone B can be largely explained by the northward advection caused by cyclone A induced southerly flow (see the left column of Figure 9) during the second time period.

As the two cyclones became increasingly closer to each other due partly to the continued environmental-flow advection of cyclone A and partly to the enhanced cyclone-cyclone interaction, their cyclone-cyclone interaction evolved nonlinearly toward the final vortex merger in the third period from 0600 UTC to 2400 UTC 20 November

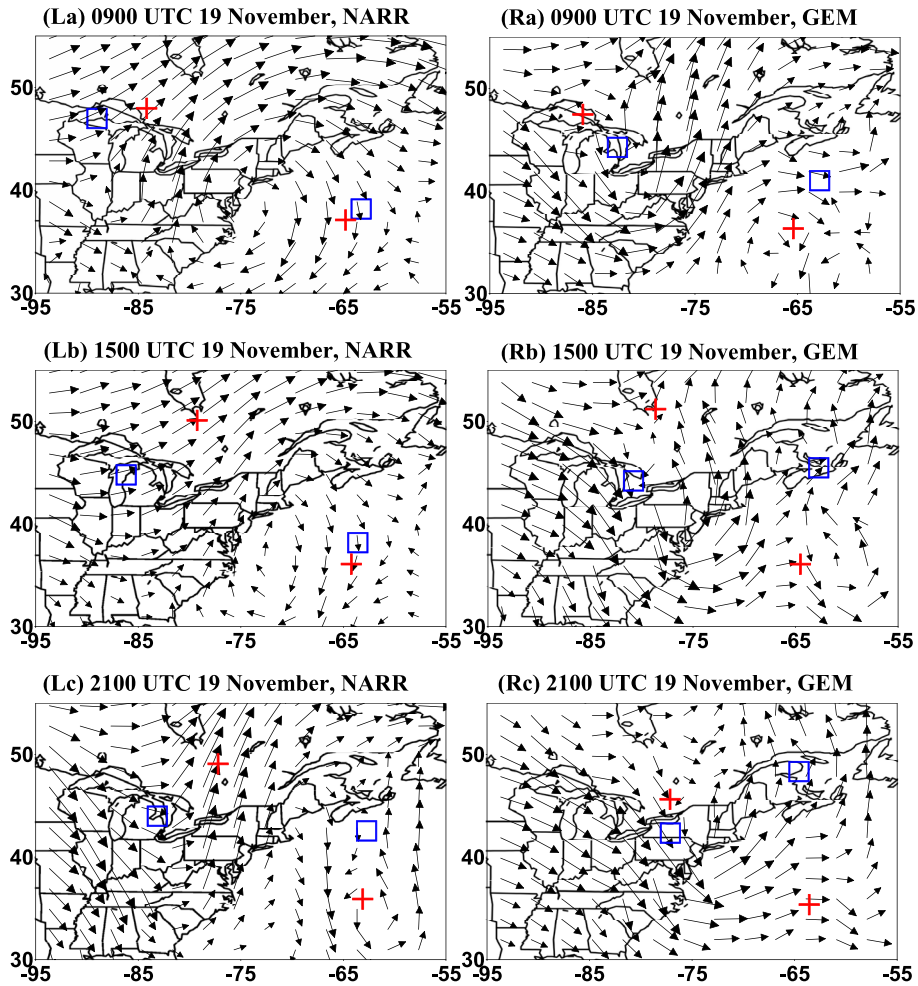

Figure 6. Same as Figure 4 except for 500 hPa. The small blue boxes mark the 500-hPa vortex center. The wind speed ranges are, respectively, (La) 1.0–49.4 m s^{-1}, (Lb) 1.0–52.6 m s^{-1}, (Lc) 1.0–49.3 m s^{-1}, (Ra) 1.0–54.7 m s^{-1}, (Rb) 1.0–48.0 m s^{-1}, and (Rc) 1.0–61.0 m s^{-1}.

(see the brown crosses that mark the merged vortex centers in Figure 1a). This vortex-merger process, started from the second period and ended in the third period, may be loosely explained based on the two-dimensional vortex merger dynamics (Yasuda & Flier1, 1995, 1997). The detailed analyses on this aspect, however, are beyond the scope of the current study, because the most intense snowfall occurred before the merger of the two cyclones.

3.2. Deviated Movements and Displaced Locations of Cyclones A and B in GEM

An analysis indicates significant differences in the movements and locations of cyclones A and B between the NARR analysis and the GEM model predictions. Although the GEM also showed the cyclone A moving northeastward and the cyclone B traveling southwestward over the first time period, the movement of the 1,000-hPa center of cyclone A in the GEM was less steady and much faster than that in NARR around 1200 UTC 19 November 2016 near the end of the first period (see Figure 1). As a result, the 1,000-hPa center of cyclone A in GEM was located notably further northeast than that in NARR at the end of the first period (cf. Figures 1a and 1b).

During the second time period, the movement of the 1,000-hPa center of cyclone A in the GEM became even more unsteady. In particular, as shown in Figure 1b, its center shifted southward by about 700 km in 3 hr from 1800 to 2100 UTC 19 at the beginning of the second period. This dramatic shift was caused mainly by a switch of the minimum (that defines the 1,000-hPa vortex center) from one pre-existing local minimum (see pink "+" signs in Figure 1b) to another local minimum newly emerged near the southern tip of the 1,000-hPa vortex core

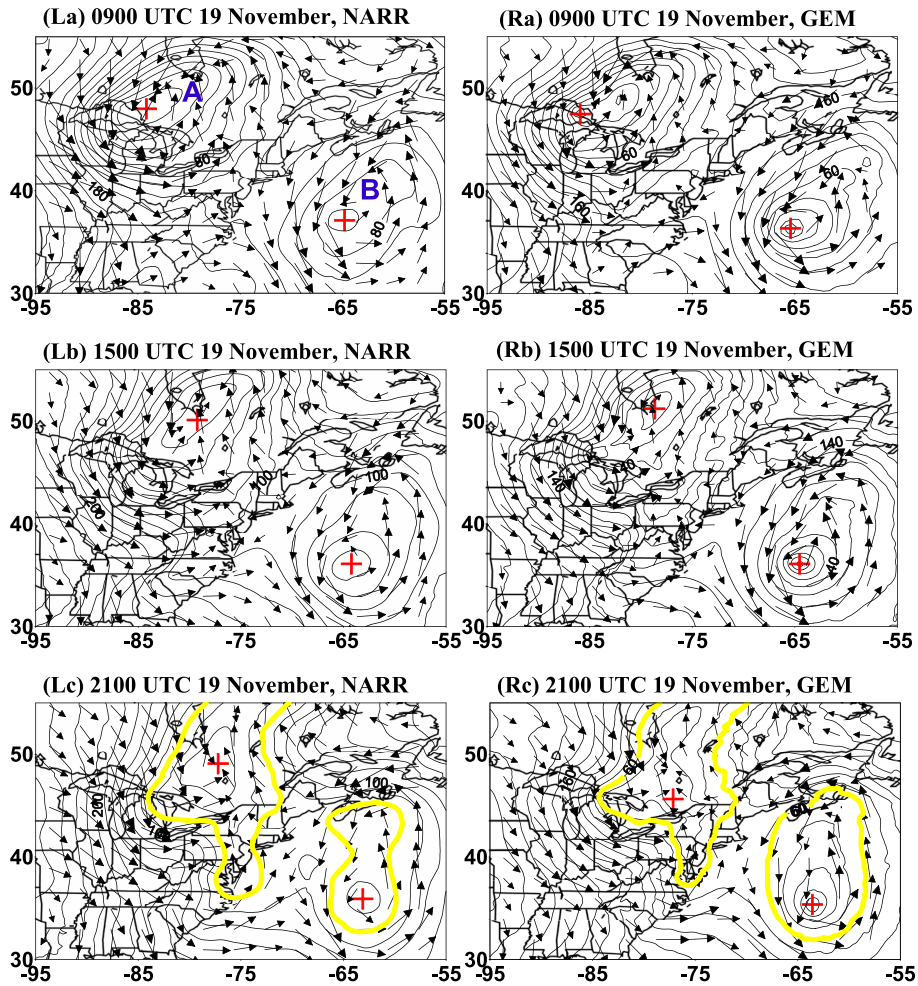

Figure 7. Same as Figure 3 except left columns for NARR and right columns for GEM 1,000-hPa geopotential height and horizontal winds at (La and Ra) 0900 UTC, (Lb and Rb) 1500 UTC, and (Lc and Rc) 2100 UTC 19 November 2016. The wind speed ranges are, respectively, (La) 1.0–21.0 m s^{-1}, (Lb) 1.0–22.2 m s^{-1}, (Lc) 1.0–21.5 m s^{-1}, (Ra) 1.0–22.3 m s^{-1}, (Rb) 1.0–21.0 m s^{-1}, and (Rc) 1.0–20.9 m s^{-1}.

area of cyclone A (see pink "+" signs in Figure 1b). As the 1,000-hPa vortex core of cyclone A in the GEM was not only moved differently but also stretched and deformed differently from that in NARR, cyclone A merged with cyclone B into a single cyclone 6 hr later in the GEM than that in NARR (see the brown crosses in Figure 1b vs. those in Figure 1a). The deviated movements and deformations of the 1,000-hPa vortex core of cyclone A in GEM compared to those in NARR caused the 1,000-hPa vortex core of cyclone A to be displaced and distorted in GEM from that in NARR. This led to the cyclone A induced flow and its interaction with cyclone B in GEM to be notably different from those in NARR, especially over Lake Erie.

In addition to the movements of 1,000-hPa cyclone A in GEM deviating from those in NARR, the movements of 500-hPa cyclone A in GEM were also different from those in NARR, especially over Lake Erie. As explained in Section 3.1 and shown in left columns of Figure 6, the NARR-analyzed cyclone A always tilted westward or southwestward against the vertical shear of environmental flow (see left columns of Figure 4), which was favorable for cyclone intensification during the period from 19 to 20 November 2016. In the GEM model, however, cyclone A did not always tilt against the vertical shear of environmental flow, indicating that the vertical structure was not always favorable for cyclone intensification (right columns of Figures 4–6, and not shown for 1800 UTC 19 and 0000 UTC 20 November). This explains why cyclone A underwent different evolution in GEM from that in NARR, so did its induced flow and interaction with cyclone B. The detailed differences of cyclone A induced flow and its interaction with cyclone B between GEM and NARR are examined in the next section.

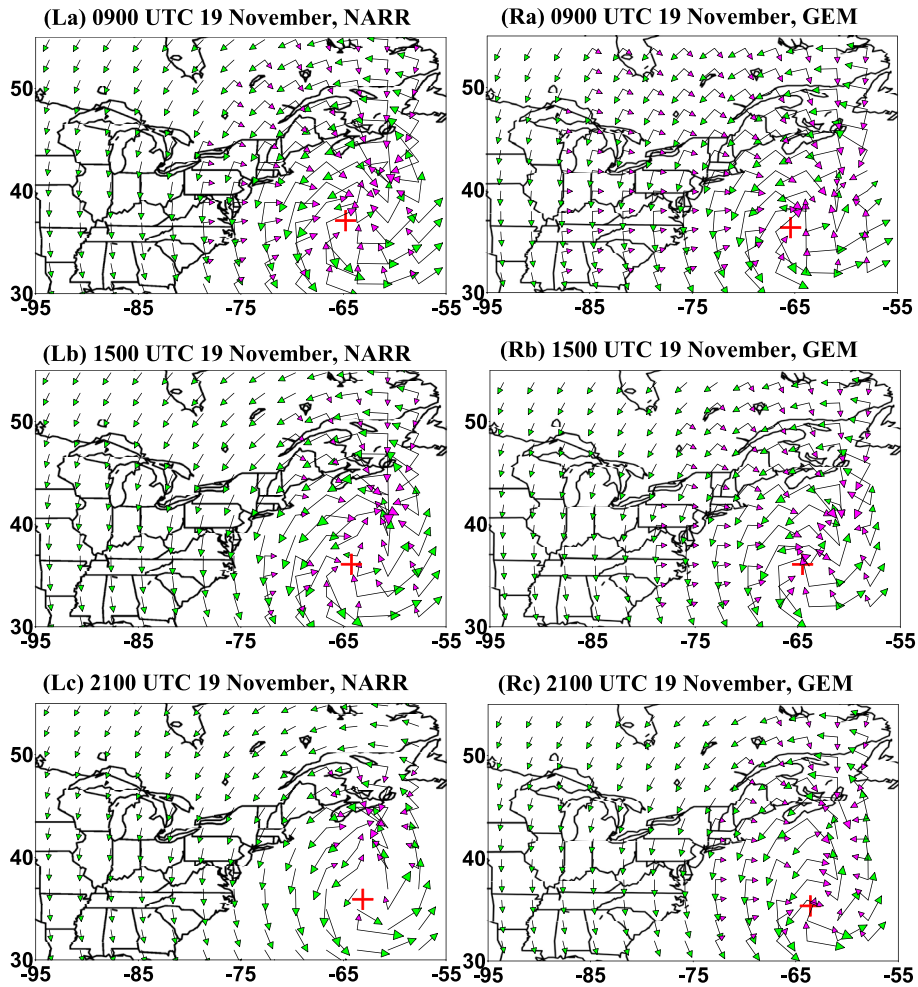

Figure 8. Same as Figure 7 except for the 1,000-hPa cyclone B induced rotational flow (m s^{-1}, in green) and divergent flow (m s^{-1}, in purple). The (rotational, divergent) speed ranges are, respectively, (La) (1.0–13.4, 1.0–5.1) m s^{-1}, (Lb) (1.0–12.7, 1.0–4.9) m s^{-1}, (Lc) (1.0–12.4, 1.0–3.3) m s^{-1}, (Ra) (1.0–19.4, 1.0–10.0) m s^{-1}, (Rb) (1.0–20.1, 1.0–8.1) m s^{-1}, and (Rc) (1.0–16.8, 1.0–7.9) m s^{-1}.

4. Different Winds and Cyclone-Induced Flows in NARR and GEM

The NARR-analyzed wind fields at 1,000 hPa (the left column of Figure 7) are compared with the GEM model predicted (the right column of Figure 7). Over Lake Erie, the GEM predicted 1,000 hPa horizontal wind is generally stronger than the NARR analyzed. For example, at 1500 UTC 19 November 2016, the GEM predicted maximum wind over Lake Erie is 14–15 m s^{-1} (northeastward) (Figure 10b), albeit close to the NARR (Figure 10a), but it covers a much larger area than that in the NARR analyzed (cf. Figures 10b and 10a). As a result, the GEM model-predicted strong wind causes more lake-effect snowfall on the lee side of Lake Erie (Figure 2) due to more latent heat flux associated with the stronger cold-dry air over the warm-moist lake surface.

Since the operational GEM model considerably over-predicts the snowbands downstream of Lake Erie (Figures 2a and 2c) during 19–20 November 2016, we will pay a close attention to the lake-effect snowfall featured with very narrow bands on the lee side of Lake Erie over this time period. As compared to the analyzed precipitation (Figure 2b), the operational GEM model over-predicted 24-hr accumulated precipitation with a maximum difference of about 20 mm (Figure 2c) over Lake Erie. Informed by 6-hr precipitation analysis, the heaviest lake-effect snowfall occurred in two time periods: 1200 UTC to 1800 UTC 19 November and 1800 UTC 19 to 0000 UTC 20 November.

Location differences of 500-hPa cyclones especially for cyclone A between the NARR analysis (left columns of Figure 5) and the GEM model prediction (right columns of Figure 5) result in differences of wind fields over

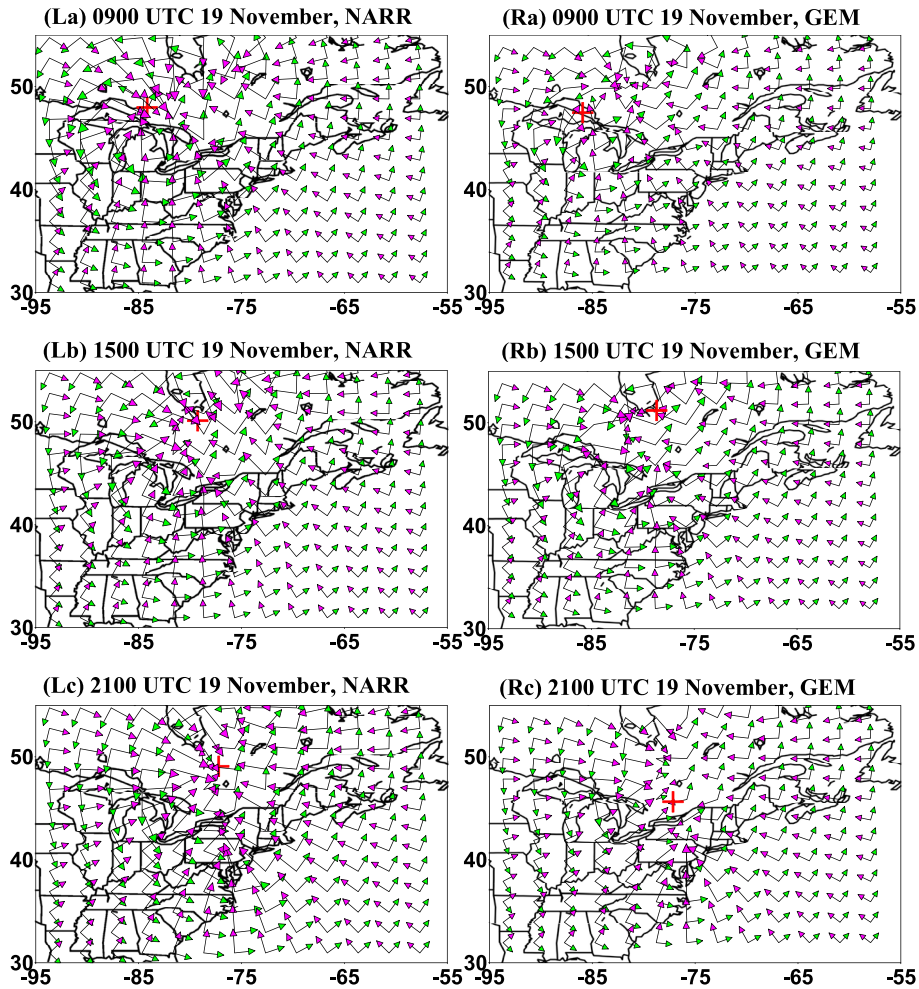

Figure 9. Same as Figure 7 except for the 1,000-hPa cyclone A induced rotational flow (m s^{-1}, in green) and divergent flow (m s^{-1}, in purple). The (rotational, divergent) speed ranges are, respectively, (La) (1.0–14.1, 1.0–10.5) m s^{-1}, (Lb) (1.0–14.0, 1.0–10.3) m s^{-1}, (Lc) (1.0–13.4, 1.0–9.4) m s^{-1}, (Ra) (1.0–18.2, 1.0–14.3) m s^{-1}, (Rb) (1.0–13.2, 1.0–10.4) m s^{-1}, and (Rc) (1.0–19.7, 1.0–9.6) m s^{-1}.

Lake Erie. At 1500 UTC 19 November over Lake Erie, for example, the GEM predicted 500-hPa total wind is 23–26 m s^{-1} (southward) (Figure 5Rb), which is weaker than the NARR analyzed wind of 36 m s^{-1} (northward) (Figure 5Lb). The substantial wind speed reduction and wind direction change in the GEM is basically due to cyclone A positioning to the northeast of Lake Erie (Figure 5Rb) whereas in the NARR, it is located to the far northwest of Lake Erie, that is, in the northern portion of Lake Michigan (Figure 5Lb).

In the following subsection, we will examine the contribution of the cyclone induced winds and their interactions to the corresponding total wind fields over Lake Erie since winds especially low-level winds determine how much latent heat flux deriving from the lake and lake-effect snowfall thereby.

4.1. Cyclone-Induced Flows and Their Interactions in NARR

Left columns of Figures 9 and 8 show the rotational (in green) and divergent (in purple) flows induced by cyclones A and B at 1,000 hPa, which are inverted from the relative vorticity and divergence fields of the NARR-analyzed wind fields. It is evident from the left columns of Figures 9 and 8 that the rotational flow is generally larger than the divergent flow for cyclone A, even though they are of the same order of magnitude. Also, cyclone A induced rotational and divergent flows decrease rapidly away from the vortex core. Evidently, the divergent flow induced by 1,000-hPa cyclone A is substantial due to the boundary-layer frictional effects (the left column of Figure 9).

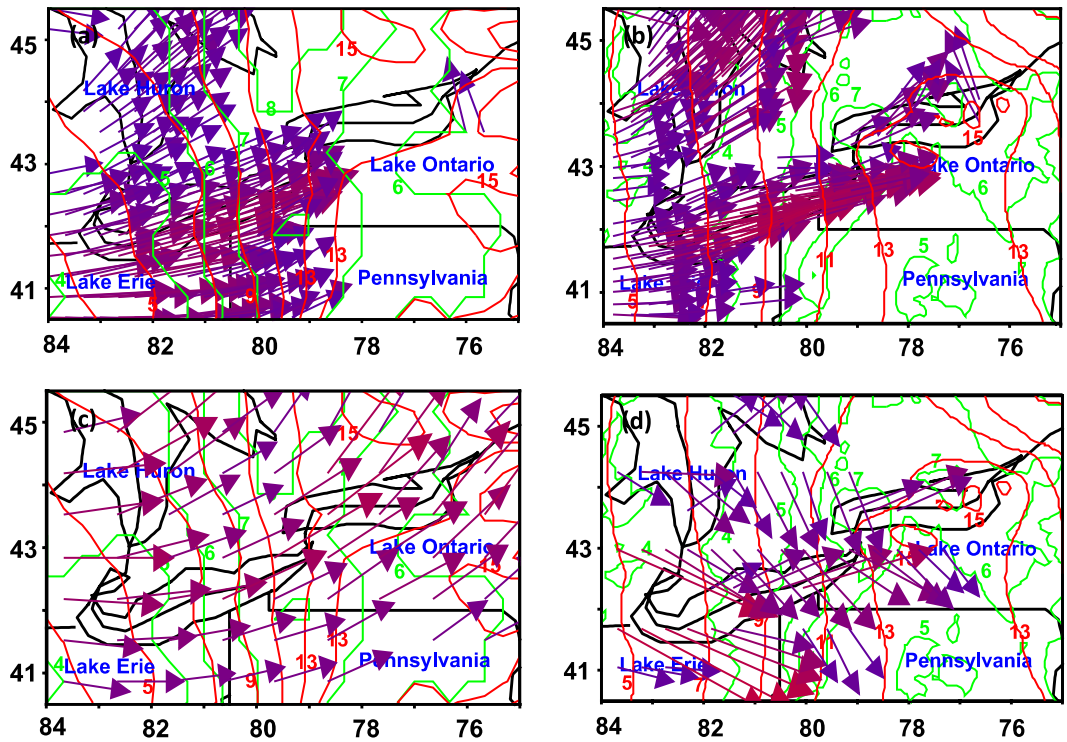

Figure 10. Left columns for NARR and right columns for GEM 1,000-hPa temperature (red solid line, in °C), specific humidity (green solid line, in g kg^{-1}) and velocity vector of total wind of (a) and (b) and cyclone A and B induced wind (c) and (d) with a wind speed range of 8.0–22.0 m s^{-1} at 1500 UTC 19 November.

However, 1,000-hPa cyclone B induced rotational flow is 2–4 times in magnitude stronger than its induced divergent flow, and the latter diminishes more quickly away from its vortex core than the former (see the left column in Figure 8), due to the less frictional effects over ocean surfaces.

A comparison of the cyclone A and B induced rotational and divergent winds with the NARR analyzed total winds at 1,000-hPa would help us understand their relative contributions to lake-effect snowfall around Lake Erie, since the low-level winds determine the magnitude of latent heat flux deriving from warm-moist water surface. For example, at 0900 UTC 19 November, the NARR cyclone A induced rotational wind was 8 m s^{-1} (eastward) and divergent wind was about 6 m s^{-1} (northward) (Figure 9La), resulting in its induced wind of about 10 m s^{-1} (northeastward), whereas cyclone B induced rotational wind was about 3 m s^{-1} (southwestward) and divergent wind was small (Figure 8La). Combining the two cyclone induced winds leads to 7 m s^{-1} (northeastward), which is about 70% of the total wind (northeastward) in Lake Erie (i.e., 10 m s^{-1}, see Figure 7La). This indicates that in the NARR, cyclones A and B induced velocities are dominant in the total velocity over Lake Erie. Similarly, at 1500 UTC 19 November, the NARR cyclone A and B induced wind is about 11 m s^{-1} (northeastward) (Figure 10c), which is about 79% of the total wind (14 m s^{-1}, northeastward) (Figure 10a).

At 2100 UTC 19 November, the NARR cyclone A induced rotational wind was 7 m s^{-1} (southeastward) and divergent wind was 5 m s^{-1} (northeastward) (Figure 9Lc) while cyclone B induced divergent wind speed was small but its induced rotational wind was about 2 m s^{-1} (southwestward) (Figure 8Lc), which partially offset the cyclone A induced divergent wind of 5 m s^{-1} (northeastward) resulting in 3 m s^{-1} (northeastward). As for the southeastward component wind, the cyclone A induced rotational wind (7 m s^{-1}) is about 78% of the total wind (i.e., 9 m s^{-1}, see Figure 7Lc). In short, the 1,000-hPa cyclone A and B induced wind in the NARR is dominant in the total winds over Lake Erie, especially at 0900, 1500, and 2100 UTC 19 November 2016.

At 500 hPa, from 0900 UTC to 2100 UTC 19 November, the net winds induced by cyclones A and B are southwesterly and southerly over Lake Erie. For example, at 1500 UTC 19 November, the two cyclone induced net wind (31 m s^{-1}, mainly southerly, see Figure 11c) is about 86% of the total wind (i.e., 36 m s^{-1} southerly, see Figure 11a).

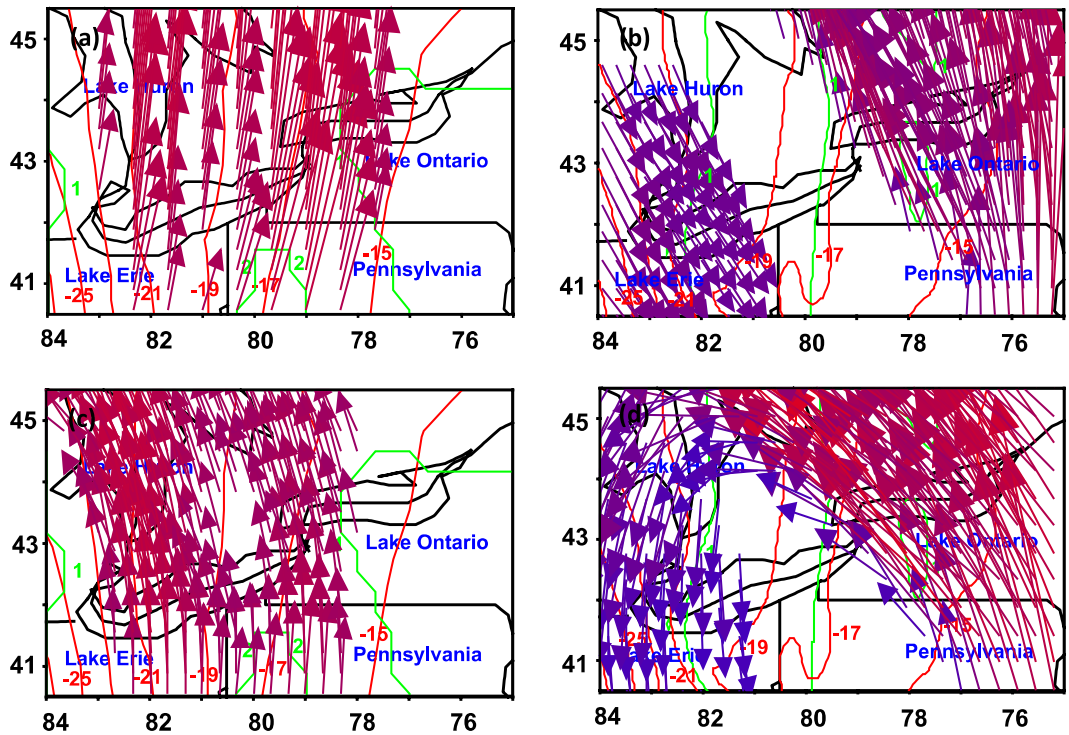

Figure 11. Left columns for NARR and right columns for GEM 500-hPa temperature (red solid line, in °C), specific humidity (green solid line, in g kg^{-1}) and velocity vector of total wind of (a) a wind speed range of 36.0–43.0 m s^{-1} and (b) a wind speed range of 23.0–43.0 m s^{-1}, and cyclone A and B induced wind of (c) a wind speed range of 25.0–43.0 m s^{-1} and (d) a wind speed range of 13.0–43.0 m s^{-1} at 1500 UTC 19 November.

4.2. Cyclone-Induced Flows and Their Interactions in GEM

Right columns of Figures 9 and 8 display the rotational (in green) and divergent (in purple) flows induced by 1,000-hPa cyclones A and B, inverted from the relative vorticity and divergence fields of the GEM predicted wind fields. A comparison of the cyclone induced winds between the NARR and the GEM model shows that both rotational and divergent flows induced by cyclones A and B in the GEM are generally stronger than those in the NARR (cf. left and right columns of Figures 9 and 8). Like the cyclone induced winds in the NARR, the GEM cyclone A induced rotational and divergent flows are of the same order of magnitude although the former is stronger than the latter (Figure 9). Both the rotational and divergent flows induced by cyclone A decrease quickly away from the vortex core. On the other hand, the cyclone B induced rotational flow is about twice in magnitude larger than its induced divergent flow, and the latter decreases away from its vortex core faster than the former (Figure 8).

Similarly, we examine the GEM 1,000-hPa cyclone A and B induced rotational and divergent winds over Lake Erie to understand the relative contribution of both cyclone induced winds and their interactions to the total wind and the lake-effect snowfall thereby. For example, at 0900 UTC 19 November, the GEM cyclone A induced rotational wind was 9 m s^{-1} (eastward), and divergent wind was 2 m s^{-1} (northeastward) (Figure 9Ra) whereas the cyclone B induced rotational wind was about 4 m s^{-1} (southwestward) and divergent wind was about 1 m s^{-1} (southeastward) (Figure 8Ra). Cyclone A's divergent wind of 2 m s^{-1} (northeastward) offset by cyclone B's rotational wind of 4 m s^{-1} (southwestward) gives rise to 2 m s^{-1} (southwestward), together with cyclone B's divergent wind of 1 m s^{-1} (southeastward), resulting in component winds of about 2.1 m s^{-1} (southward) and 0.7 m s^{-1} (westward). Hence, the net winds induced by two cyclones over Lake Erie have components of 8.3 m s^{-1} (eastward) and 2.1 m s^{-1} (southward), where the eastward component wind is about 92% of the total wind (eastward) over Lake Erie (i.e., 9 m s^{-1}, see Figure 7Ra). Furthermore, these eastward and southward winds indicate flows coming from west and north directions, bring relative cold and dry air over Lake Erie. In contrast, at the same time in the NARR cyclones A and B induced net wind of about 7 m s^{-1} (northeastward) conveys relative warm and moist air from south and west directions over Lake Erie (cf. Figures 9La and 9Ra, and 8La and 8Ra).

At 1500 UTC 19 November over eastern portion of Lake Erie, the GEM 1,000-hPa cyclone A induced rotational wind was 8 m s^{-1} (northeastward) and divergent wind was 4 m s^{-1} (northeastward) (Figure 9Rb), leading to total cyclone A induced wind of 12 m s^{-1} (northeastward). On the other hand, over the western portion of Lake Erie, 1,000-hPa cyclone A induced rotational wind was 6 m s^{-1} (southeastward) (Figure 9Rb) and 1,000-hPa cyclone B induced rotational wind was about 4 m s^{-1} (southwestward) and its divergent wind speed was very small (Figure 8Rb), resulting in the induced net wind in southeastward direction. Over the eastern portion of Lake Erie, the net winds induced by cyclones A and B over Lake Erie are about 12 m s^{-1} (northeastward), 86% of total wind (i.e., 14 m s^{-1}, northeastward, see Figure 7Rb). As shown in Figure 10d, both northeastward and southeastward winds carry relative cold and dry air induced by two cyclones over warm and moist Lake Erie. However, the NARR 1,000-hPa cyclone A and B induced net wind is about 11 m s^{-1} (northeastward) (Figure 10c), about 79% of the total wind (14 m s^{-1}, northeastward) (Figure 10a), transporting less dry and cold air than the GEM over Lake Erie (cf. Figures 10b and 10d). In short, the cyclone A and B induced winds at 1,000 hPa over Lake Erie in the GEM were essentially stronger than those in the NARR and so was their resulting evaporation over Lake Erie.

At 500 hPa over Lake Erie the cyclone induced winds in the GEM were dominated by cyclone A induced rotational wind during the period from 0900 UTC 19 November to 0000 UTC 20 November 2016 (not shown), as observed in the NARR. However, the 500-hPa cyclone induced wind directions above Lake Erie varied more dramatically in GEM than in NARR, because the 500-hPa vortex center of cyclone A underwent more dramatic location changes relative to Lake Erie in GEM than in NARR (see the small blue boxes in left columns vs. right columns of Figure 6). In summary, during the major lake-effect snowfall periods such as at 1500 UTC 19 November 2016, the 500-hPa cyclone A and B induced winds over Lake Erie were mainly northerly in the GEM (e.g., Figure 11d), but mostly southerly in the NARR (e.g., Figure 11c), which contribute to their total winds in the GEM (Figure 11b) and the NARR (Figure 11a), respectively. Since the GEM total wind is northwesterly (Figure 11b) but the NARR total wind is southerly (Figure 11a), the GEM predicts much strong 500-hPa cold advection than the NARR, suggesting that the former produce more vertical temperature gradients and potentially more atmospheric instability than the latter.

5. Errors in GEM Predicted CSI Compared With NARR

Over Lake Erie, the GEM overly predicted the CSI occurrences especially during the heavy snowfall period. For example, at 1500 UTC 19 November, the GEM predicted CSI covered much broader areas around Lake Erie (Figure 12Ra) than the CSI areas in the NARR (Figure 12La). In the GEM, the maximum CSI release index of 3 was distributed at lee of Lake Erie as well as in Lake Erie (Figure 12Ra). In the NARR, however, the maximum CSI release index of 3 was only located over Lake Erie (Figure 12La). Again, at 2100 UTC 19 November, the GEM predicted CSI covered increasingly larger and broader areas in and near Lake Erie (Figure 12Rb) than the CSI areas in the NARR (Figure 12Lb). In the former, the area includes the majority of Lake Erie and large area to south of Lake Erie with the maximum CSI release index of 4 (Figure 12Rb). In the latter, on the other hand, the CSI areas mainly contain lee areas of Lake Erie located to south of western Lake Erie and to east of Lake Erie with the maximum CSI release index of 3 (Figure 12Lb). It is interesting to note that the areas of CSI occurrence in the NARR during intensive snowfall period (e.g., 2100 UTC 19 and 0000 UTC 20 November) well match lake-effect snowfall located to south and east of Lake Erie (cf. Figures 2b and 2s. 12Lb and 12Lc). At 0000 UTC 20 November 2016, the GEM over-predicted CSI with the maximum CSI release index of 4 over large areas of lee of Lake Erie (Figure 12Rc) while the NARR-analyzed the maximum CSI release index was only 3 over Lake Erie (Figure 12Lc). These over-predicted CSI occurrences in the GEM largely explain the false alarm of the severe lake-effect snowfall in Lake Erie.

We further compare the CSI release index daily accumulation from 1200 UTC 19 November to 1200 UTC 20 November 2016 between the NARR and the GEM. To test if our computation of CSI release index is sensitive to the GEM model high horizontal grid spacing, we perform the experiment by resampling the original 10-km horizontal grid spacing GEM model prediction data onto 30-km grids, which is close to the NARR horizontal grid spacing of 32 km. As shown in Figure 13, the GEM consistently over-predicted CSI occurrence particularly over Lake Erie where accumulated CSI release index in the GEM ranges from 15 to 18 (Figure 13b) but in the NARR it only varies from about 9 to 12 (Figure 13a).

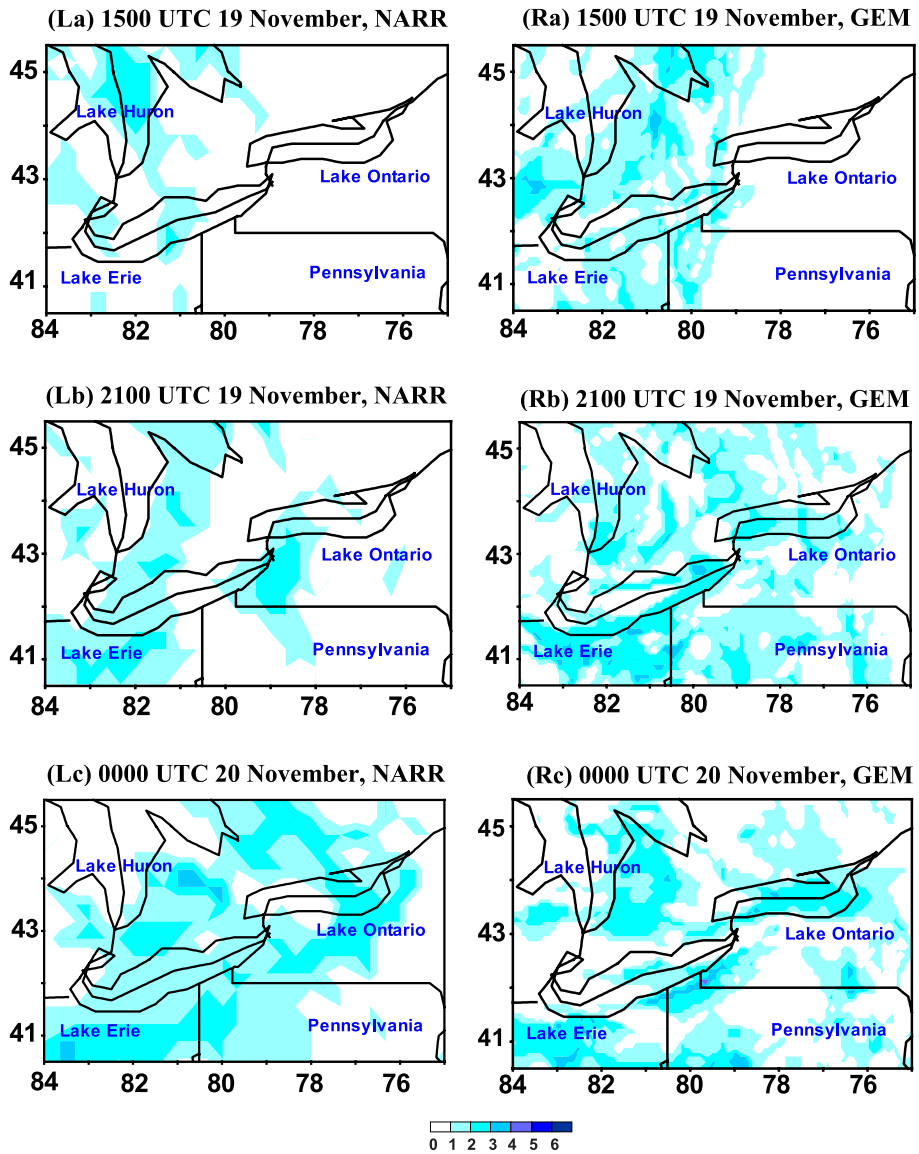

Figure 12. Left columns for NARR and right columns for GEM CSI release index over the Great Lakes region at (La and Ra) 1500 UTC, (Lb and Rb) 2100 UTC 19, and (Lc and Rc) 0000 UTC 20 November 2016.

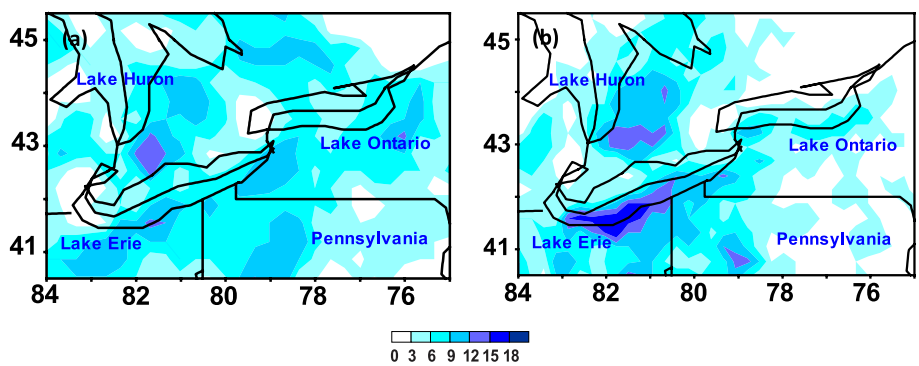

Figure 13. The CSI release index accumulation from 1200 UTC 19 November to 1200 UTC 20 November 2016 of (a) the NARR including CI, and (b) the GEM 30-km horizontal resolution including CI.

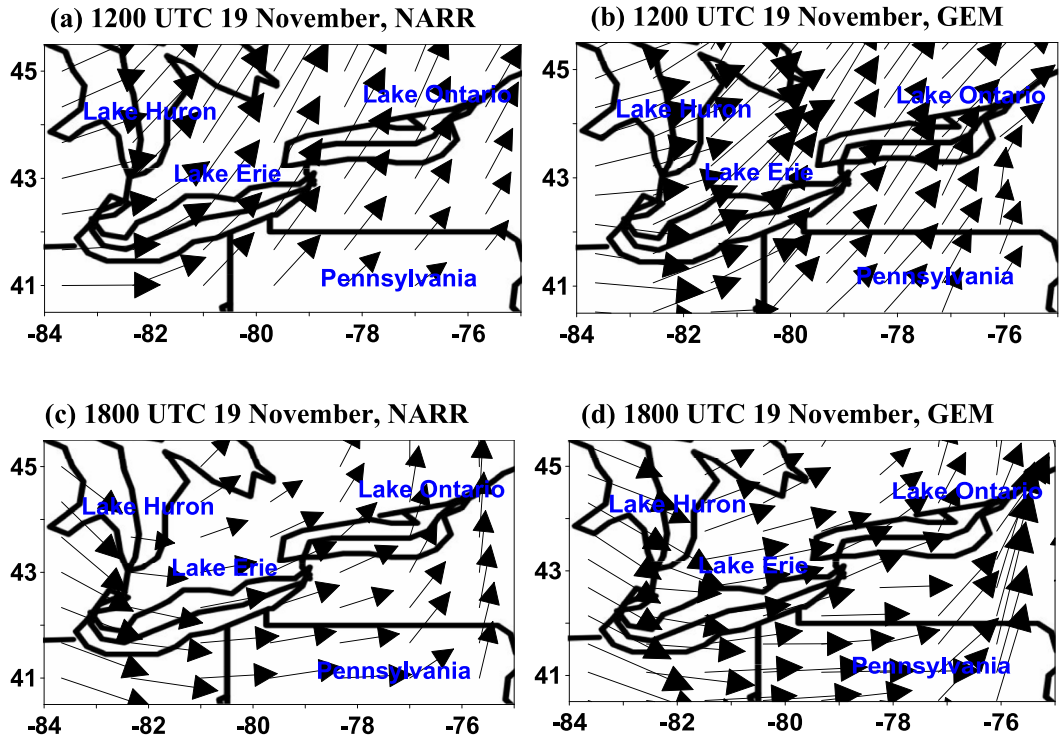

Figure 14. Left columns for NARR and right columns for GEM 850-hPa horizontal winds at (a) 1200 UTC 19 November 2016 with a wind speed range of 8.0–26.3 m s^{-1}, (b) 1200 UTC 19 November 2016 with a wind speed range of 8.0–29.0 m s^{-1}, (c) 1800 UTC 19 November 2016 with a wind speed range of 8.0–32.9 m s^{-1}, and (d) 1800 UTC 19 November 2016 with a wind speed range of 8.0–29.3 m s^{-1}.

6. Discussion

Based on forecast experiences in the United States and Canada, Niziol (1987), Murphy (1989), and Cotton (1990) summarized the following common favorable thermodynamic and dynamic conditions for the development of lake-effect snowfall in the Great Lakes region: (a) the temperature difference between the lake surface and 850-hPa equals or exceeds 13°C, (b) the height of low-level inversion exceeds 1 km, (c) an onshore wind has an overwater fetch of more than 100 km or 150 km (Cotton, 1990; Murphy, 1989), and (d) low-level wind speeds over lake surfaces should be moderate to strong (Cotton, 1990). The first two conditions are implicitly included in our 3-D MPV computation, while the latter two are directly considered in our study through total wind and cyclone-induced rotational and divergent components as well as their interactions.

To see if the low-level flow between the boundary layer and 700 hPa informs the snow bands' orientation, we plot 850-hPa winds from the NARR and GEM in Figure 14, showing that they are almost parallel to the leeside shorelines of Lake Erie. This is consistent with the snowband orientation shown in Figure 2. At 1200 UTC 19 November, over and at leeside of Lake Erie the horizontal winds in the NARR are about 13 m s^{-1} (Figure 14a) whereas they are around 17 m s^{-1} in the GEM (Figure 14b). A similar situation occurs at 1800 UTC 19 November with 14 m s^{-1} in the NARR (Figure 14c) but 16 m s^{-1} in the GEM (Figure 14d). The stronger winds in the GEM than those in the NARR indicates that over and at the leeside of Lake Erie the wind differences between 850-hPa and 1,000-hPa in the GEM (10 m s^{-1} at 1200 UTC, and 6 m s^{-1} at 1800 UTC) are larger than those in the NARR (5 m s^{-1} at 1200 UTC, and 3 m s^{-1} at 1800 UTC). As discussed above, this wind shear difference leads to CSI that is stronger in the GEM (Figure 13b) than in the NARR (Figure 13a) and more lake-effect snowfall in the GEM than what was observed (Figure 2c).

Furthermore, we have computed the CSI release index that includes three elements of instability, moisture availability, and lifting condition. The triggering mechanism can involve topographic lifting (e.g., Campbell et al., 2016; Campbell & Steenburgh, 2017), frictional lifting, thermal lifting and dynamic lifting (Steenburgh & Campbell, 2017). Besides, one of the unique features of our study is to extract divergent flows induced by

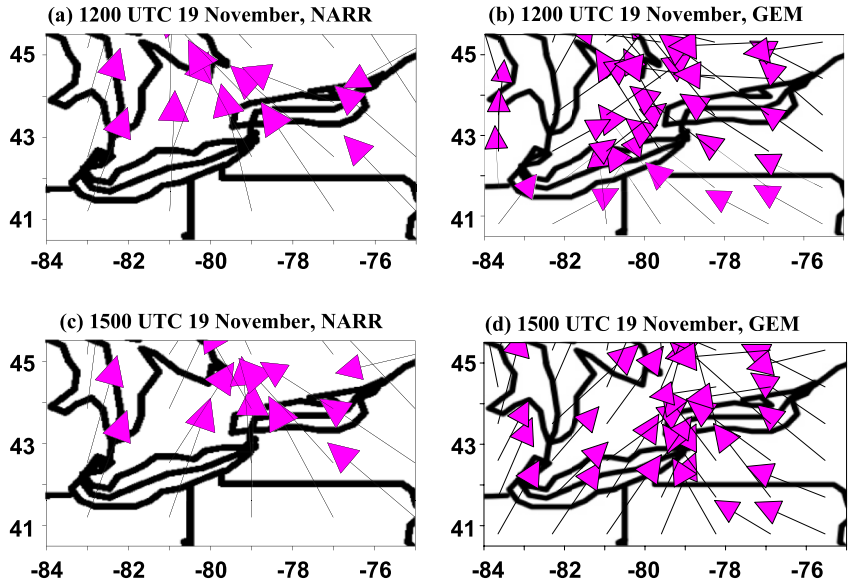

Figure 15. Left columns for NARR and right columns for GEM 1,000-hPa cyclone A induced divergent flow (m s^{-1}, in purple) at (a) 1200 UTC 19 November 2016 with a wind speed range of 1.0–10.6 m s^{-1}, (b) 1200 UTC 19 November 2016 with a wind speed range of 1.0–11.9 m s^{-1}, (c) 1500 UTC 19 November 2016 with a wind speed range of 1.0–10.3 m s^{-1}, and (d) 1500 UTC 19 November 2016 with a wind speed range of 1.0–10.4 m s^{-1}.

cyclones and to see where and when these flows contribute dynamic convergence and vertical motion. As shown in Figure 15, cyclone A induced divergent flows in the GEM demonstrate stronger convergence than those in the NARR at and near lee side of Lake Erie at 1200 UTC and 1500 UTC 19 November (cf. Figures 15a and 15b, and 15c, 15d). This can contribute to GEM's false alarm for the lake-effect snowfall case examined in this study.

As shown in Figure 16a, negative MPV, as a necessary condition of CSI, is observed from 1,000 hPa to 800 hPa surfaces covering the entire horizontal extent, whereas CCI within the CSI regions is mainly located below 850 hPa. Since the thermal wind is unidirectional or nearly so, the CCI above the boundary layer (or even surface

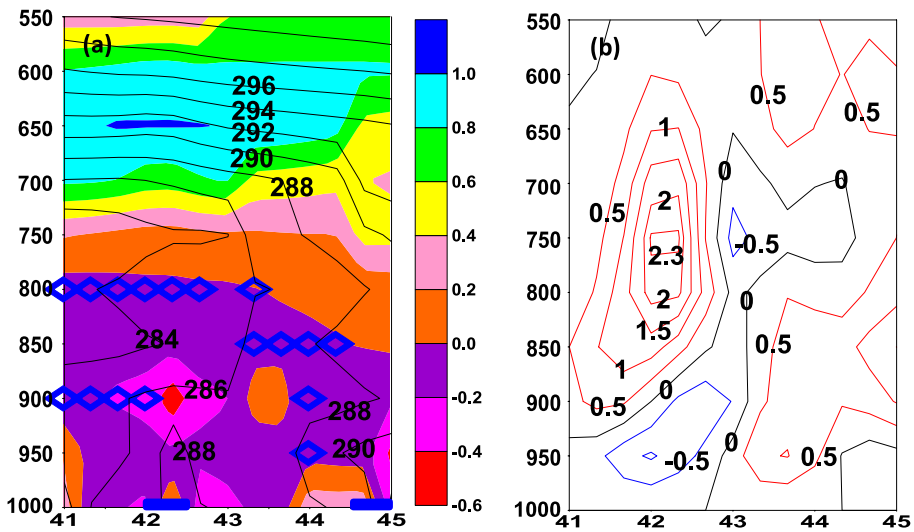

Figure 16. (a) NARR vertical cross sections along −80.2°W (the abscissa is in latitude °N with thick blue lines denoting Lake Erie (left) and Georgian Bay (right), and the ordinate is in hPa) of moist potential vorticity with color shading (at 0.1 PVU intervals), locations of non-zero CSI release index denoted by blue diamonds, and equivalent potential temperature (K) drawn by black contours at 0000 UTC 20 November 2016. (b) Same as (a) except for vertical motion (cm s^{-1}; positive and negative for upward and downward motion respectively).

layer) is not pure CCI (for exactly upright convection) but can be considered as CSI (even in the limit of vanishing thermal wind). With this understanding, the clouds (if found) above 850 hPa should be generated by CSI and have their roots on the lake boundary layer. Based on vertical distributions of negative MPV and equivalent potential temperature shown in Figure 16a, to south of 43°N (Lake Erie over 42°N–42.5°N) CCI exists below 850 hPa where the equivalent potential temperature decreases with height by about 2–4°C from 950 to 850 hPa. Above 850 hPa, however, the equivalent potential temperature increases with height by nearly 1°C from 850 to 800 hPa and about 2°C from 750 to 700 hPa. This indicates that CCI is relatively strong below 850 hPa but rapidly decreases its strength with height, and becomes CCI neutral or near stable in the well-mixed layer above 850 hPa. At and above 850 hPa mainly CSI is present (Figure 16a). This is consistent with Milrad et al.'s (2011) findings, indicating that the convection is nearly upright at low levels but become increasingly slantwise at upper levels above the region of CCI. At lee side of Georgian Bay (between 43°N and 44.5°N), CSI release (denoted by blue diamonds) occurs in the neighborhood of 950 hPa where the equivalent potential temperature decreases with height by about 1°C, in the neighborhood of 900 hPa where the equivalent potential temperature increases with height less than 1°C, and in the neighborhood of 850 and 800 hPa where the equivalent potential temperature almost has no changes. This indicates that CCI is near stable or close to neutral states from 900 to 800 hPa. From a horizontal distribution perspective, CSI release index is dominant at lee side of Lake Erie (south of 42°N) at 900 and 800 hPa, over Lake Erie (between 42°N and 42.5°N) at 900, and 800 hPa, over the land and at lee side of Georgian Bay (south of 44.5°N) at 950, 900, 850, and 800 hPa (Figure 16). Hence, CSI release indeed responds for formation of lake-effect snowfall (cf. Figures 16 and 2b).

Performing PV inversion is beyond the scope of the current study since the PV inversion and Cao et al. (2019)'s diagnostic method are two different methods. First, Cao et al. (2019)'s diagnostic method directly inverts wind fields from relative vorticity and divergence so that it is easy to use and computationally fast. Second, this method deals with both rotational and divergent flows induced by the vorticity and divergence, respectively, in the core area of each cyclone but the PV inversion only deals with the rotational flows. More importantly, the PV method has the following issues: (a) the uniqueness and the existence of solutions for the PV inversion system cannot be proved mathematically; (b) the system equations cannot be classified as elliptic, hyperbolic, or parabolic due to their nonlinearity unless forcing PV anomalies being positive (e.g., Davis & Emanuel, 1991) or introducing an arbitrary parameter in the equations to control (Wang & Zhang, 2003); (c) arbitrarily partitioning total PV anomalies into pieces may result in discontinuities at edges of each piece and violation of a superposition principle (e.g., Egger, 2008; Kieu & Zhang, 2010; Røsting & KristjÁnsson, 2012); (d) N pieces of PV require 2N times of simultaneous iterations for nonlinear partial differential equations although the iteration numbers may be reduced to N by applying an algorithm developed by Kieu and Zhang (2010), and large number of iterations is time consuming and may lead to numerical instability; (e) choices of the mean reference state cannot avoid arbitrariness. However, the advantage of PV inversion method is to simultaneously invert 3-D rotational flows given balanced and boundary conditions. To obtain 3-D rotational and divergent flows inverted from the vorticity and divergence, respectively, in the core area of each cyclone, Cao et al. (2019)'s diagnostic method can be easily extended into a 3-D version via an approach of inverting flows layer (2-D) by layer (2-D). This simple 3-D extension, however, is purely kinematical, which is an intrinsic limitation of the method.

7. Summary and Conclusions

In this study, the cyclone-cyclone interactions and their impacts on a lake-effect snowfall event over the Great Lakes region are examined using our recently-developed method (Cao et al., 2019). This event was a false alarm that the Canadian operational model predicted the snowfall on the lee of Lake Erie with an amount twice as much as the analyzed precipitation.

This false alarm lake-effect snowfall event involved two cyclones (A and B) and their mutual interactions with the environmental flow. The cyclones A and B predicted by the operational model were situated at unfavorable locations at both low and upper levels, resulting in inaccurate prediction of cyclone A and B induced winds and their resulting interactions over Lake Erie. At 1,000 hPa, the inaccurate prediction of the two cyclone induced winds and their resulting interactions over Lake Erie led to colder and drier air carried over warm and moist lake surface with more latent heat flux deriving from the open lake surface. At 500 hPa, there were considerable location differences of two cyclones between the NARR and the GEM, resulting in the 500-hPa cyclone A and B induced winds during the intense snowfall period over Lake Erie mainly northerly in the GEM but southerly in the NARR.

In addition to dynamics associated with cyclone induced winds especially at the low level, we have further investigated the vertically integrated physical processes at all possible levels, including both dynamic and thermodynamic processes. The CSI release index is a good candidate to satisfy these requirements since it well represents the vertically integrated dynamic and thermodynamic process. Besides, CSI is likely a good physical mechanism for formation of precipitation bands. At low levels of Lake Erie both CCI and CSI are present whereas at upper levels and lee side of the lake only CSI is present. It is found in this study that CSI index, representative of CSI release, is dominant at lee side of Lake Erie, as well as upper levels of Lake Erie and over the land. CSI release indeed responds for formation of lake-effect snowfall.

By computing and analyzing CSI release index, we have shown that the differences in CSI were responsible for different development of snowbands over Lake Erie between the NARR and the GEM. In general, the GEM over-predicted CSI intensity and area coverage. Over Lake Erie during the intense snowfall period, the GEM over-predicted CSI with the maximum daily accumulated CSI release index up to 18 in and on the lee of Lake Erie whereas the NARR-analyzed maximum daily accumulated CSI release index was about 12 over Lake Erie. The GEM over-predictions of CSI occurrences led to the false alarm of the lake-effect snowfall over Lake Erie with large errors in precipitation especially in its intensity.

In short, as a consequence of the GEM model predicting 1,000-hPa cyclones in wrong locations, the low-level winds (induced by two cyclones and their interactions) become too cold and too dry over Lake Erie, and these lead to excessive evaporation from the lake which generates excessive available potential energy for CCI (below 850 hPa) and CSI (above 850 hPa). Furthermore, as the GEM model predicted 500-hPa cyclone positions are dramatically deviated from the observed ones, the upper-level winds (induced by two cyclones and their interactions) become northerly over Lake Erie opposite to the observed southerly winds, and these generate excessive vertical shears in the GEM, which give rise to excessive CSI (above 850 hPa). As a result, we have observed that the GEM over-prediction of CSI (including CCI) occurrences, and the false alarm of lake-effect snowbands over Lake Erie since CSI is a likely physical mechanism forming precipitation bands (e.g., Bennetts & Hoskins, 1979; Clark et al., 2002; Lussky, 1989; Xu, 1986, 1992; Zhang & Cho, 1992).

The lake-effect snowfall event examined in this paper is concerned with the GEM model prediction errors in two cyclone locations at low- and upper-levels. The location errors are likely associated with the model initial conditions, for example, one of the substantial location errors occurred at 12 UTC 19 November 2016 when the model integration just began. It is suggested to improve the GEM data assimilation system in order to incorporate more observations from both meteorological organizations and non-meteorological organizations such as airlines and conservation authorities.

It has been shown that our recently-developed diagnostic method is useful not only for summer but also for winter cases, as demonstrated in Cao et al. (2019) and the current work. We anticipate that this method can and will be applied to more cases associated with cyclone-cyclone interactions as well as to operational model post-processes to detect and resolve problems related to cyclone interaction through decomposing model predicted flows into cyclone- or vortex-induced flows and the remaining environmental flows. Since our decomposition technique is a diagnostic method that helps us to understand the important contributing factor to lake-effect snowfall, it cannot be used alone to foresee a potential false alarm. On the other hand, if significant location errors of model-predicted cyclones can be foreseen or assessed beforehand by using additional sources of information (such as model-predicted ensemble spreads with properly projected biases of predicted cyclone locations), then our decomposition technique can be used as a supplementary tool to identify the potential false alarm on lake-effect snowfalls in future applications. This could be an important subject for future work.

In addition, as demonstrated in this paper, using the CSI index to detect CSI occurrence can provide comprehensive information for precipitation predicting and post-processing in an operational numerical weather prediction system.

Data Availability Statement

The operational GEM regional model predictions and Canadian Precipitation Analysis (CaPA) are available from the Canadian Meteorological Centre or the website of https://github.com/julemai/CaSPAr/wiki/Available-products. NCEP North American Regional Reanalysis (NARR) data provided by the NOAA PSL, Boulder, Colorado, USA, from their website at https://psl.noaa.gov/data/gridded/data.narr.html.

Acknowledgments
We would like to thank Drs. Stéphane Bélair, and Junhua Zhang for carefully reading an earlier version of the manuscript and providing constructive suggestions. We also thank three anonymous reviewers for their constructive suggestions and comments that have helped improve the quality of this paper. We appreciate Dr. Lin Zhu's assistance in obtaining the NARR digital data.

References

Ballentine, R. J., Stamm, A. J., Chermack, E. E., Byrd, G. P., & Schleede, D. (1998). Mesoscale model simulation of the 4-5 January 1995 lake-effect snowstorm. *Weather Forecasting*, *13*(4), 893–920. https://doi.org/10.1175/1520-0434(1998)013<0893:mmsotj>2.0.co;2

Barnes, L. R., Gruntfest, E. C., Hayden, M. H., Schultz, D. M., & Benight, C. (2007). False alarm and close calls: A conceptual model of warning accuracy. *Weather Forecasting*, *22*(5), 1140–1147. https://doi.org/10.1175/waf1031.1

Batchelor, G. K. (1980). *An introduction to fluid dynamics* (5th ed., p. 615). Cambridge University Press.

Becker, E. J., Berbery, E. H., & Higgins, R. W. (2009). Understanding the characteristics of daily precipitation over the United States using the North American regional reanalysis. *Journal of Climate*, *22*(23), 6268–6286. https://doi.org/10.1175/2009jcli2838.1

Bennetts, D. A., & Hoskins, B. J. (1979). Conditional symmetric instability - A possible explanation for frontal rainbands. *Quaterly Journal of the Royal Meteorological Society*, *105*(446), 945–962. https://doi.org/10.1002/qj.49710544615

Brotzge, J., Erickson, S., & Brooks, H. (2011). A 5-yr climatology of tornado false alarms. *Weather Forecasting*, *26*(4), 534–544. https://doi.org/10.1175/waf-d-10-05004.1

Bukovsky, M. S., & Karoly, D. J. (2007). A brief evaluation of precipitation from the North American regional reanalysis. *Journal of Hydrometeorology*, *8*(4), 837–846. https://doi.org/10.1175/jhm595.1

Burnett, A. W., Kirby, M. E., Mullins, H. T., & Patterson, W. P. (2003). Increasing Great Lake-effect snowfall during the twentieth century: A regional response to global warming? *Journal of Climate*, *16*(21), 3535–3542. https://doi.org/10.1175/1520-0442(2003)016<3535:igIsdt>2.0.co;2

Campbell, L. S., & Steenburgh, W. J. (2017). The OWLeS IOP2b snowstorm: Mechanisms contributing to the Tug Hill precipitation maximum. *Monthly Weather Review*, *145*(7), 2461–2478. https://doi.org/10.1175/MWR-D-16-0461.1

Campbell, L. S., Steenburgh, W. J., Veals, P. G., Letcher, T. W., & Minder, J. R. (2016). Lake-effect mode and precipitation enhancement over the Tug Hill plateau during OWLeS IOP2b. *Monthly Weather Review*, *144*(5), 1729–1748. https://doi.org/10.1175/MWR-D-15-0412.1

Cao, J., & Xu, Q. (2011). Computing stream function and velocity potential in a limited domain of arbitrary shape. Part II: Numerical methods and test experiments. *Advances in Atmospheric Sciences*, *28*(6), 1445–1458. https://doi.org/10.1007/s00376-011-0186-5

Cao, Z., Belair, S., & Zhang, D.-L. (2022). The impact of incorporating the air-lake interaction on the quantitative precipitation forecasts over southern Ontario. *Weather Forecasting*, *37*(8), 1471–1490. https://doi.org/10.1175/waf-d-21-0187.1

Cao, Z., & Cho, H.-R. (1995). Generation of moist potential vorticity in extratropical cyclones. *Journal of the Atmospheric Sciences*, *52*(18), 3263–3282. https://doi.org/10.1175/1520-0469(1995)052<3263:gompvi>2.0.co;2

Cao, Z., Xu, Q., & Zhang, D.-L. (2019). A new method to diagnose cyclone-cyclone interaction and its influences on precipitation. *Journal of Applied Meteorology Climatology*, *58*(8), 1821–1851. https://doi.org/10.1175/jamc-d-18-0344.1

Cao, Z., & Zhang, D.-L. (2004). Tracking surface cyclones using moist potential vorticity. *Advances in Atmospheric Sciences*, *21*(5), 830–835. https://doi.org/10.1007/BF02916379

Cao, Z., & Zhang, D.-L. (2016). Analysis of missed summer severe rainfall forecasts. *Weather Forecasting*, *31*(2), 433–450. https://doi.org/10.1175/WAF-D-15-0119.1

Carrera, M. L., Gyakum, J. R., & Lin, C. A. (2009). Observational study of wind channeling within the St. Lawrence River valley. *Journal of Applied Meteorology Climatology*, *48*(11), 2341–2361. https://doi.org/10.1175/2009jamc2061.1

Clark, J. H. E., James, R. P., & Grumm, R. H. (2002). A reexamination of the mechanisms responsible for banded precipitation. *Monthly Weather Review*, *130*(12), 3074–3086. https://doi.org/10.1175/1520-0493(2002)130<3074:arotmr>2.0.co;2

Côté, J., Gravel, S., Méthot, A., Patoine, A., Roch, M., & Staniforth, A. (1998). The operational CMC/MRB global environmental multiscale (GEM) model: Part I – Design considerations and formulation. *Monthly Weather Review*, *126*(6), 1373–1395. https://doi.org/10.1175/1520-0493(1998)126<1373:tocmge>2.0.co;2

Cotton, W. R. (1990). *Storms. Geophysical science series* (Vol. 1, p. 158pp). ASTeR Press.

Davis, C. A., & Emanuel, K. A. (1991). Potential vorticity diagnostics of cyclogenesis. *Monthly Weather Review*, *119*(8), 1929–1953. https://doi.org/10.1175/1520-0493(1991)119<1929:pvdoc>2.0.co;2

Egger, J. (2008). Piecewise potential vorticity inversion: Elementary tests. *Journal of the Atmospheric Sciences*, *65*(6), 2015–2024. https://doi.org/10.1175/2007jas2564.1

Ellis, A. W., & Johnson, J. J. (2004). Hydroclimatic analysis of snowfall trends associated with the North American Great Lakes. *Journal of Hydrometeorology*, *5*(3), 471–486. https://doi.org/10.1175/1525-7541(2004)005<0471:haosta>2.0.co;2

Fortin, V., Roy, G., Donaldson, N., & Mahidjiba, A. (2015). Assimilation of radar quantitative precipitation estimations in the Canadian Precipitation Analysis (CaPa). *Journal of Hydrology*, *531*, 296–307. https://doi.org/10.1016/j.jhydrol.2015.08.003

Fujisaki-Manome, A., Mann, G. E., Anderson, E. J., Coauthors, P. Y., Fitzpatrick, L. E., Benjamin, S. G., et al. (2020). Improvements to lake-effect snow forecast using a one-way air-lake model coupling approach. *Journal of Hydrometeorology*, *21*, 2813–2828. https://doi.org/10.1175/JHM-D-20-0079.1

Fujisaki-Manome, A., Wright, D. M., Mann, G. E., Anderson, E. J., Chu, P., Jablonowski, C., & Benjamin, S. G. (2022). Forecasting lake-/sea-effect snowstorms, advancement, and challenges. *WIREs Water*, *9*(4), e1594. https://doi.org/10.1002/wat2.1594

Huang, M., Cao, Z., & Shen, X. (2019). A study on the relationship between conditional symmetric instability and northward jumping of the summer monsoon rainband in east China. *Chinese Journal of Atmospheric Sciences*, *43*(5), 943–958.

Isard, S. A., Angel, J. R., & VanDyke, G. T. (2000). Zones of origin for Great lakes cyclones in North America, 1899-1996. *Monthly Weather Review*, *128*(2), 474–485. https://doi.org/10.1175/1520-0493(2000)128<0474:zoofgl>2.0.co;2

Keshishian, L. G., Bosart, L. F., & Bracken, W. E. (1994). Inverted troughs and cyclogenesis over interior North America: A limited regional climatology and case studies. *Monthly Weather Review*, *122*(4), 565–607. https://doi.org/10.1175/1520-0493(1994)122<0565:itacoi>2.0.co;2

Kieu, C. Q., & Zhang, D.-L. (2010). A piecewise potential vorticity inversion algorithm and its application to hurricane inner-core anomalies. *Journal of the Atmospheric Sciences*, *67*(8), 2616–2631. https://doi.org/10.1175/2010JAS3421.1

Kocin, P. J., & Uccellini, L. W. (1990). *Snowstorms along the northeastern coast of the United States: 1955 to 1985. Meteorology Monograph, No. 44* (p. 280). American Meteorological Society.

Kristovich, D. A., Young, G. S., Verlinde, J., Sousounis, P. J., Mourad, P., Lenschow, D., et al. (2000). The lake-induced convection experiment and the snowband dynamics project. *Bulletin of American Meteorological Society*, *81*(3), 519–542. https://doi.org/10.1175/1520-0477(2000)081<0519:tlceat>2.3.co;2

Kuo, H. L. (1961). Convection in a conditionally unstable atmosphere. *Tellus*, *13*(4), 441–459. https://doi.org/10.3402/tellusa.v13i4.9516

Lai, C.-C., & Bosart, L. F. (1988). A case study of trough merger in split westerly flow. *Monthly Weather Review*, *116*(10), 1838–1856. https://doi.org/10.1175/1520-0493(1988)116<1838:acsotm>2.0.co;2

Laird, N. F., Kristovich, D. A. R., & Walsh, J. E. (2003). Idealized model simulations examining the mesoscale structure of winter lake-effect circulations. *Monthly Weather Review*, *131*(1), 206–221. https://doi.org/10.1175/1520-0493(2003)131<0206:imsetm>2.0.co;2

Langlois, A., Kohn, J., Royer, A., Cliche, P., Brucker, L., Picard, G., et al. (2009). Simulation of snow water equivalent (SWE) using thermodynamic snow models in Quebec, Canada. *Journal of Hydrometeorology*, *10*(6), 1447–1463. https://doi.org/10.1175/2009jhm1154.1

Lespinas, F., Fortin, V., Roy, G., Rasmussen, P., & Stadnyk, T. (2015). Performance evaluation of the Canadian precipitation analysis (CaPA). *Journal of Hydrometeorology*, *16*(5), 2045–2064. https://doi.org/10.1175/JHM-D-14-0191.1

Lilly, D. K. (1960). On the theory of disturbances in a conditionally unstable atmosphere. *Monthly Weather Review*, *88*, 1–17. https://doi.org/10.1175/1520-0493(1960)088<0001:ottodi>2.0.co;2

Lussky, G. R. (1989). Heavy rains and flooding in Montana: A case for operational use of symmetric instability diagnosis. *Weather Forecasting*, *4*(2), 186–201. https://doi.org/10.1175/1520-0434(1989)004<0186:hrafim>2.0.co;2

Mahfouf, J.-F., Brasnett, B., & Gagnon, S. (2007). A Canadian precipitation analysis (CaPA) project: Description and preliminary results. *Atmosphere-Ocean*, *45*, 1–17. https://doi.org/10.3137/ao.v450101

Mann, G. E., Wagenmaker, R. B., & Sousounis, P. J. (2002). The influence of multiple lake interactions upon lake-effect storms. *Monthly Weather Review*, *130*(6), 1510–1530. https://doi.org/10.1175/1520-0493(2002)130<1510:tiomli>2.0.co;2

Mesinger, F., DiMego, G., Kalnay, E., Mitchell, K., Shafran, P. C., Ebisuzaki, W., et al. (2006). North American regional reanalysis. *Bulletin of the American Meteorological Society*, *87*(3), 343–360. https://doi.org/10.1175/BAMS-87-3-343

Milrad, S. M., Gyakum, J. R., Atallah, E. H., & Smith, J. F. (2011). A diagnostic examination of the eastern Ontario and Western Quebec wintertime convection event of 28 January 2010. *Weather Forecasting*, *26*(3), 301–318. https://doi.org/10.1175/2010waf2222432.1

Murphy, B. P. (1989). The lake effect snowstorm of 5-6 January 1988 in southern Ontario. *Ontario Region Technical Notes*, *8*, 89–95. Available from Downsview library.

Niziol, T. A. (1987). Operational forecasting of lake effect snowfall in Western and central New York. *Weather Forecasting*, *2*(4), 310–321. https://doi.org/10.1175/1520-0434(1987)002<0310:ofoles>2.0.co;2

Niziol, T. A., Snyder, W. R., & Waldstreicher, J. S. (1995). Winter weather forecasting throughout the eastern United States. Part IV: Lake effect snow. *Weather Forecasting*, *10*(1), 61–77. https://doi.org/10.1175/1520-0434(1995)010<0061:wwftte>2.0.co;2

Norton, D. C., & Bolsenga, S. J. (1993). Spatiotemporal trends in lake effect and continental snowfall in the Laurentian Great Lakes, 1951-1980. *Journal of Climate*, *6*(10), 1943–1956. https://doi.org/10.1175/1520-0442(1993)006<1943:stilea>2.0.co;2

Payer, M., Laird, N. F., Maliawco, R. J., Jr., & Hoffman, E. G. (2011). Surface fronts, troughs, and baroclinic zones in the Great Lakes region. *Weather Forecasting*, *26*(4), 555–563. https://doi.org/10.1175/waf-d-10-05018.1

Røsting, B., & KristjÁnsson, J. E. (2012). The usefulness of piecewise potential vorticity inversion. *Journal of the Atmospheric Sciences*, *69*(3), 934–941. https://doi.org/10.1175/jas-d-11-0115.1

Steenburgh, W. J., & Campbell, L. S. (2017). The OWLeS IOP2b snowstorm: Shoreline geometry and the mesoscale forcing of precipitation. *Monthly Weather Review*, *145*(7), 2421–2436. https://doi.org/10.1175/MWR-D-16-0460.1

Tardy, A. (2000). *Lake effect and lake enhanced snow in the Champlain Valley of Vermont. Eastern region technical attachment, No. 2000-05* (p. 27). NOAA/National Weather Service.

Wang, X., & Zhang, D.-L. (2003). Potential vorticity diagnosis of a simulated hurricane. Part I: Formulation and quasi-balanced flow. *Journal of the Atmospheric Sciences*, *60*(13), 1593–1607. https://doi.org/10.1175/2999.1

Wiggin, B. L. (1950). Great snows of the Great lakes. *Weatherwise*, *3*(6), 123–126. https://doi.org/10.1080/00431672.1950.9927065

Wright, D. M., Posselt, D. J., & Steiner, A. L. (2013). Sensitivity of lake-effect snowfall to lake ice cover and temperature in the Great Lakes region. *Monthly Weather Review*, *141*(2), 670–689. https://doi.org/10.1175/MWR-D-12-00038.1

Xu, Q. (1986). Conditional symmetric instability and mesoscale rainbands. *Quarterly Journal of the Royal Meteorological Society*, *112*(472), 315–334. https://doi.org/10.1002/qj.49711247203

Xu, Q. (1992). Formation and evolution of frontal rainbands and geostrophic potential vorticity anomalies. *Journal of the Atmospheric Sciences*, *49*(8), 629–648. https://doi.org/10.1175/1520-0469(1992)049<0629:faeofr>2.0.co;2

Xu, Q., & Clark, J. H. E. (1985). The nature of symmetric instability and its similarity to convective and inertial instability. *Journal of the Atmospheric Sciences*, *42*(24), 2880–2883. https://doi.org/10.1175/1520-0469(1985)042<2880:tnosia>2.0.co;2

Yasuda, I., & Flier1, G. R. (1995). Two dimensional asymmetric vortex merger: Contour dynamics experiment. *Journal of Oceanography*, *51*(2), 145–170. https://doi.org/10.1007/bf02236522

Yasuda, I., & Flierl, G. R. (1997). Two-dimensional asymmetric vortex merger: Merger dynamics and critical merger distance. *Dynamics of Atmospheres and Oceans*, *26*(3), 159–181. https://doi.org/10.1016/s0377-0265(96)00485-x

Zhang, D.-L., & Cho, H.-R. (1992). The development of negative moist potential vorticity in the stratiform region of a simulated squall line. *Monthly Weather Review*, *120*(7), 1322–1341. https://doi.org/10.1175/1520-0493(1992)120<1322:tdonmp>2.0.co;2

Ziv, B., & Alpert, P. (1995). Rotation of binary cyclones – A data analysis study. *Journal of the Atmospheric Sciences*, *52*(9), 1357–1369. https://doi.org/10.1175/1520-0469(1995)052<1357:robcda>2.0.co;2